



# Critical Level of Nitrogen Incorporation in Silicon Oxynitride Films: Transition of Structure and Properties, toward Enhanced Anticorrosion Performance

Konstantina Topka, Babacar Diallo, Maxime Puyo, Paris Papavasileiou, Charlotte Lebesgue, Cecile Genevois, Yann Tison, Cedric Charvillat, Diane Samelor, Raphael Laloo, et al.

## ► To cite this version:

Konstantina Topka, Babacar Diallo, Maxime Puyo, Paris Papavasileiou, Charlotte Lebesgue, et al.. Critical Level of Nitrogen Incorporation in Silicon Oxynitride Films: Transition of Structure and Properties, toward Enhanced Anticorrosion Performance. ACS Applied Electronic Materials, 2022, 4 (4), pp.1741 - 1755. 10.1021/acsaelm.2c00018 . hal-03657402

**HAL Id: hal-03657402**

**<https://hal.science/hal-03657402>**

Submitted on 3 May 2022

**HAL** is a multi-disciplinary open access archive for the deposit and dissemination of scientific research documents, whether they are published or not. The documents may come from teaching and research institutions in France or abroad, or from public or private research centers.

L'archive ouverte pluridisciplinaire **HAL**, est destinée au dépôt et à la diffusion de documents scientifiques de niveau recherche, publiés ou non, émanant des établissements d'enseignement et de recherche français ou étrangers, des laboratoires publics ou privés.

# **Critical level of nitrogen incorporation in silicon oxynitride films: Transition of structure and properties, towards enhanced anticorrosion performance**

Konstantina Christina Topka<sup>1,2</sup>, Babacar Diallo<sup>3</sup>, Maxime Puyo<sup>4</sup>, Paris Papavasileiou<sup>1</sup>, Charlotte Lebesgue<sup>4</sup>, Cecile Genevois<sup>3</sup>, Yann Tison<sup>5</sup>, Cedric Charvillat<sup>1</sup>, Diane Samelor<sup>1</sup>, Raphael Laloo<sup>4</sup>, Daniel Sadowski<sup>1</sup>, François Senocq<sup>1</sup>, Thierry Sauvage<sup>3</sup>, Hugues Vergnes<sup>2</sup>, Marie-Joelle Menu<sup>4</sup>, Brigitte Caussat<sup>2</sup>, Viviane Turq<sup>4</sup>, Nadia Pellerin<sup>3</sup>, Constantin Vahlas<sup>1,\*</sup>

<sup>1</sup> CIRIMAT, CNRS-INP-UPS, ENSIACET, Toulouse INP, 4 Allée Emile Monso, BP 44362, 31030 Toulouse cedex 4 – France

<sup>2</sup> Laboratoire de Génie Chimique (LGC), Université de Toulouse, CNRS, 4 Allée Emile Monso, CS 84234, Toulouse cedex 4, 31432, France

<sup>3</sup> CEMHTI, CNRS UPR3079, 1D avenue de la Recherche Scientifique, 45071 Orleans, cedex 2, France

<sup>4</sup> CIRIMAT, CNRS-INP-UPS, Université Toulouse 3 - Paul Sabatier, 118 Route de Narbonne, 31062 Toulouse cedex 9 - France

<sup>5</sup> Université de Pau et des Pays de l'Adour, E2S UPPA, CNRS, IPREM, Pau, France Helioparc Pau - Pyrenees, 2 Avenue du President Angot, 64053 Pau Cedex 9, France

\*Corresponding author: [constantin.vahlas@ensiacet.fr](mailto:constantin.vahlas@ensiacet.fr)

CIRIMAT, CNRS-INP-UPS, ENSIACET, Toulouse INP, Toulouse, France

## **Abstract**

Silicon oxynitride ( $\text{SiO}_x\text{N}_y$ ) thin films are widely encountered in today's major Key Enabling Technologies. Exhibiting tunable properties dependent on the nitrogen content, they attract attention in applications requiring thermal stability, high dielectric constant, corrosion resistance, surface passivation and effective ion diffusion barrier. Identification of the minimum desired level of nitrogen incorporation for each application is important for simultaneously optimizing material properties and deposition process. In this context, we study the structural and functional properties of  $\text{SiO}_x\text{N}_y$  films

deposited from tris(dimethylsilyl)amine (TDMSA), O<sub>2</sub> and NH<sub>3</sub>, using conveniently scalable atmospheric pressure chemical vapor deposition (CVD) at moderate temperature (600–650°C). A suite of characterization techniques including spectroscopic ellipsometry (SE), Fourier-transform infrared spectroscopy (FT-IR), ion beam analyses (IBA), nanoindentation, nanoscratch, X-ray photoelectron spectroscopy (XPS), high-resolution transmission electron microscopy (HR-TEM), water wettability, surface roughness and resistance to wet etching corrosion are implemented in order to establish the relevant structure-composition-properties correlations. The produced SiO<sub>x</sub>N<sub>y</sub> films are smooth and amorphous, exhibiting beyond state-of-the art corrosion resistance in standard though particularly aggressive hydrofluoric buffer oxide etchant (BOE) 6:1 solution, with remarkable near-zero etching rate values. Compositional trends reveal the presence of C and H atoms, yet their incorporation has insignificant effect on the films RMS roughness and wet etching corrosion resistance. Coupled SE, FT-IR and XPS analyses reveal that the SiO<sub>x</sub>N<sub>y</sub> network appears to undergo a sharp transition between 4–6 at.% N, affecting hardness and Young's modulus. Globally, material properties such as scratch resistance, surface roughness and corrosion resistance are improved with increasing nitrogen content. Additionally, the asymmetric stretching silicon nitride (Si<sub>3</sub>N<sub>4</sub>) FT-IR absorption at ca. 850 cm<sup>-1</sup> is used to track the binding configuration in the amorphous SiO<sub>x</sub>N<sub>y</sub> network. Correlation of the elemental environment and chemical bonding to the corresponding process conditions can aid in identifying the process margins for desired intrinsic and/or functional properties.

**Keywords:** Silicon oxynitride, tris(dimethylsilyl)amine, chemical vapor deposition, buffer oxide etchant, hydrolysis resistance, thin film, material network, wet etching corrosion,

## Abbreviations

AFM: atomic force microscope

ALD: atomic layer deposition

ARC: anti-reflective coatings

BEMA: Bruggeman effective medium approximation

BOE: buffer oxide etchant

CAE: constant analyzer energy

CCD: charge-coupled device

CFD: computational fluid dynamics

CMOS: complementary metal-oxide-semiconductor

CVD: chemical vapor deposition

DR: deposition rates

EELS: electron energy loss spectroscopy

ERDA: elastic recoil detection analysis

FIB: focused ion beam

FT-IR: Fourier-transform infrared spectroscopy

FWHM: full width half maximum

HR-TEM: high-resolution transmission electron microscopy

IBA: ion beam analyses

LED: light emitting devices

MIR/NIR: mid- and near infrared

NRA: nuclear reaction analysis

PECVD: plasma enhanced chemical vapor deposition

RBM: random binding model

RBS: Rutherford backscattering spectroscopy

RMM: random mixture model

RMS: root mean square

SE: spectroscopic ellipsometry

SEM: scanning electron microscope

SPT: set-point temperature

STEM-HAADF: scanning transmission electron microscopy-high angle annular dark field

Si<sub>3</sub>N<sub>4</sub>: silicon nitride

SiC: silicon carbide

SiO<sub>2</sub>: silicon dioxide

SiO<sub>x</sub>N<sub>y</sub>: silicon oxynitride

TDMSA: tris(dimethylsilyl)amine

TO3/LO3: transverse and longitudinal optical symmetric stretching vibrations of the Si-O-Si bond

WCA: water contact angle

XPS: X-ray photoelectron spectroscopy

sccm: standard cubic centimeters per minute

## Introduction

Silicon oxynitride (SiO<sub>x</sub>N<sub>y</sub>) films have gathered increasing attention in international technology policy concepts such as the recent Key Enabling Technologies European Union one.<sup>1</sup> With structure and properties transitioning from stoichiometric silica (SiO<sub>2</sub>) to silicon nitride (Si<sub>3</sub>N<sub>4</sub>),<sup>2</sup> amorphous SiO<sub>x</sub>N<sub>y</sub> films have been widely used in the fields of micro- and opto-electronics<sup>3</sup>. They have especially garnered attention since early 2000s as high-k replacements for the classical SiO<sub>2</sub> gate dielectrics.<sup>4</sup> Their denser network in comparison to SiO<sub>2</sub> lends them promising scratch-resisting, encapsulation, anti-corrosion and ion diffusion-limiting properties, finding them a spot in applications such as Na and B diffusion

barriers in light emitting devices (LED)<sup>5</sup>, passivation film on surface acoustic wave devices<sup>6</sup> or at the TiO<sub>2</sub>/SiON/n-Si gate-stacks for advanced CMOS devices<sup>7</sup>, and for hard encapsulation of carbon dots<sup>8</sup>. Their oxygen permeability and low water vapor transmission rate is also in demand for food packaging and electronic devices,<sup>9</sup> given their ability to prevent degradation or failure of chemically reactive electrodes or conductive components after exposure to humidity or oxygen. Although this material has been widely studied due to the above outstanding properties, further investigation of the structural and chemical disorder is of essence for new upcoming applications of SiO<sub>x</sub>N<sub>y</sub>.<sup>10</sup> Moreover, control of the chemical composition of such films is essential. Adjustable SiO<sub>x</sub>N<sub>y</sub> film composition, and by extension tunable properties such as refractive index or network density, are often achieved by controlling the starting reaction chemistry.

Throughout the past decades, several technologies have been studied for the production of SiO<sub>x</sub>N<sub>y</sub> films. Oxidation of SiN<sub>x</sub> or high-temperature nitridation and ion implantation on SiO<sub>2</sub> have been proposed as one option, typically involving thermal or plasma nitridation processes.<sup>11</sup> In addition, physical or chemical vapor deposition have also been investigated and used extensively. Conventionally, reagents such as NH<sub>3</sub> and N<sub>2</sub>O have been utilized, in combination with silicon-containing precursors such as hexamethyldisilazane (HMDS), trisilylamine (TSA), silane (SiH<sub>4</sub>) and others.<sup>12</sup> Most thermal processes however involve high temperatures (800–1200°C), resulting in films with compressive internal stresses and degraded performance.<sup>13</sup> The choice of precursors is of importance as it affects the operating thermal window, the chemical composition and properties of the resulting film. For instance, use of SiH<sub>4</sub> and NH<sub>3</sub> may produce films with relatively high hydrogen content, diffusing and generating traps in the gate dielectric,<sup>14</sup> causing decreased electrical performance.

Moreover, many of the previously described applications involve heat-sensitive and/or 3D-complex structures. Common literature that targets low deposition temperature reports SiO<sub>x</sub>N<sub>y</sub> films that are amorphous and produced by plasma enhanced chemical vapor deposition (PECVD) processes.<sup>15, 16</sup> However, increased hydrogen incorporation is often encountered in PECVD prepared films,<sup>17</sup> which can be detrimental to barrier performance. As a cost-effective alternative, atmospheric pressure thermal CVD process is proposed, operated using reactive chemistries complying with deposition at moderate temperatures, compatible with heat sensitive substrates such as glass.

In the present work, the processing of SiO<sub>x</sub>N<sub>y</sub> films from the rarely-reported tris(dimethylsilyl)amine (N(SiHMe<sub>2</sub>)<sub>3</sub>, TDMSA) precursor is studied. Selected as a potential dual source of Si and N, TDMSA is supplied in presence of NH<sub>3</sub> and/or O<sub>2</sub>. A parametric analysis based on the process conditions is carried out and the evolution of the network structure and properties is investigated as a function of the nitrogen incorporation. Combining information input from spectroscopic ellipsometry (SE), ion beam analysis (IBA), high-resolution transmission electron microscopy (HR-TEM), X-ray photoelectron spectroscopy (XPS) and Fourier transform infrared analysis (FT-IR), the

structural order and chemical characteristics are correlated to mechanical and functional properties. Finally, the link between distinct levels of nitrogen incorporation,  $N_x$ -Si- $O_z$  tetrahedral configuration and their influence on the material properties is investigated. Particular attention is paid on the interdependence between film composition and wet etching rate, targeting applications such as protective, hydrolysis-resisting coatings for glass containers or etch-stop liners in field effect transistor devices. This work is the final part of a trilogy on CVD of  $SiO_xN_y$  films. Firstly, starting with the analysis of the gas phase during  $SiO_xN_y$  deposition from the same chemistry, information on by-products and active intermediates has been collected in order to elucidate the chemical mechanism leading to film production.<sup>18</sup> Secondly, the acquired results were applied in the development of a chemical model dealing with the simulation of the  $SiO_xN_y$  deposition process for the first time, and offering grounds for process optimization studies using computational fluid dynamics (CFD) calculations.<sup>19</sup> Being the last in this collection of new information on the  $SiO_xN_y$  deposition, the present work contributes to a holistic approach of the processing, characterization and functionality of such films.

## Experimental Section

### *Films processing*

CVD of  $SiO_xN_y$  films was carried out in a horizontally aligned hot-wall reactor, illustrated in Figure SI1 of *Supporting Information*. The reaction chamber was defined by a 700 mm long quartz tube ( $\varnothing$  46 mm internal). When heated, a thermal gradient develops, as presented in Figure 1 in the Results and Discussion section, featuring a 140 mm long isothermal section spanning from 360 to 500 mm. Deposition experiments were carried out at four different set-point temperatures (SPT), i.e. 550, 580, 625 and 650°C, corresponding to the temperature of the isothermal zone of the reactor. This temperature range is significantly lower than 760-820°C that is the state of the art for atmospheric pressure thermal CVD  $SiO_xN_y$  films.<sup>20</sup> Unless specified otherwise, the majority of the analyzed samples were taken from the isothermal region, an example of which is shown exemplified in Figure 1 in the Results and Discussion section.

Three lines supplied  $N_2$  (99.9999 %, Messer),  $O_2$  (99.9995 %, Messer) and  $NH_3$  (99.999 %, Linde) gases, as illustrated in Figure SI1. The flow rates were established by mass flow controllers (Brooks 5850TR). TDMSA (95 %, abcr) was conditioned in a bubbler and was transported in the deposition zone through  $N_2$  serving as carrier gas. Details on the bubbler and carrier gas line temperatures, pressure gauges and pumping equipment have been described elsewhere.<sup>19</sup> The operating pressure was kept constant at  $9.73 \times 10^5$  Pa (730 Torr) for all runs. Thirteen experiments were realized at deposition conditions that are summarized in Table 1. It is noted that runs TD9 and TD5 supplied 0

standard cubic centimeters per minute (sccm) of O<sub>2</sub> at the inlet, however potential microleaks or H<sub>2</sub>O desorption from the reactor internal surfaces of the reaction chamber cannot be excluded.

Table 1. Experimental conditions for the production of SiO<sub>x</sub>N<sub>y</sub> films from TDMSA.

Run code	SPT (°C)	O <sub>2</sub> (sccm)	TDMSA (sccm)	O <sub>2</sub> :TDMSA flow ratio	NH <sub>3</sub> (sccm)	Deposition time (min)
TD1	550	2	6	0.33	20	30
TD2	580	2	6	0.33	20	30
TD3	650	2	6	0.33	20	150
TD4	650	2	2	1	20	150
TD5	650	-	2	-	20	150
TD6	650	0.6	2	0.3	20	150
TD7	650	0.6	2	0.3	-	150
TD8	650	0.6	2	0.3	40	150
TD9	650	-	2	-	-	150
TD10	650	0.6	2	0.3	-	900
TD11	650	0.3	2	0.15	-	225
TD12	650	1.2	2	0.6	-	150
TD14	625	0.6	2	0.3	-	300

Monocrystalline silicon (100) n-type wafers (Neyco S.A., 32 x 24 mm<sup>2</sup>) served as substrates. Their preparation, degreasing and placement in the 57-500 mm region of the reactor have been described elsewhere.<sup>21</sup> Eighteen such samples were used in each experiment; their position is exemplified in Figure 1 in the Results and Discussion section.<sup>21</sup> The sample code for each position “p” contains a letter of the alphabet (e.g. pA) for samples located outside of the isothermal region, and a number (e.g. p1) for samples located in the isothermal region of the reaction chamber.

### *Measurement of film thickness and composition*

The SiO<sub>x</sub>N<sub>y</sub> film deposition rates (DR) were calculated from thickness measurements performed by SE, using a Semilab SE-2000 instrument operating at an incidence angle of 70°. Each sample was probed at 5 points along the vertical center line as illustrated in the inset of Figure SI1 of *Supporting Information*. The SE data were fitted using a Bruggeman Effective Medium Approximation (BEMA) model in the Semilab SEA software. A three-component model was applied, comprised of SiO<sub>2</sub>, Si<sub>3</sub>N<sub>4</sub> and amorphous-C. Details on how this model was calibrated for extraction of SiO<sub>x</sub>N<sub>y</sub> film composition with non-negligible amounts of carbon are described elsewhere.<sup>19</sup> Results were deemed appropriated for a linear regression fit  $R^2 \geq 0.99$ . The average thickness (and by extension average deposition rate) and average film composition in Si, O, N and C were calculated from the aforementioned five points.

The stoichiometry of SiO<sub>x</sub>N<sub>y</sub> films was measured by coupling Rutherford Backscattering Spectroscopy (RBS) and Nuclear Reaction Analysis (NRA) techniques. Additional composition results considering the composition in H were also obtained by Elastic Recoil Detection Analysis (ERDA). These techniques are shortly referred to as ion beam analyses. The absence of other elements polluting the samples was also verified. The middle of a sample positioned at 38.4 cm from the reactor inlet (i.e. located within the isothermal region), was probed for all runs (Figure SI1 of *Supporting Information*). The composition of the films was obtained by simulation of the RBS, NRA and ERDA spectra using the SIMNRA software.<sup>22</sup> Details on the above characterizations have been described in previous publications.<sup>18, 23</sup>

### *Chemical structure*

The chemical structure of the deposited SiO<sub>x</sub>N<sub>y</sub> films was assessed in transmission mode by FT-IR (Frontier FT-IR MIR/NIR spectrometer), equipped with a custom-made substrate support that facilitated rotation of the sample in relation to the incident beam. Two angles (0° and 60°) were used in this work. After removal of the background signal, sixty four accumulations in the 400–4000 cm<sup>-1</sup> spectral range were collected for each sample with 4 cm<sup>-1</sup> resolution. Post-acquisition processing of the data included removal of the substrate signature and baseline correction. The absorbance values were normalized by the corresponding thickness of each film, given that in transmission mode, the intensities of absorptions relating to various Si–O–Si vibrational modes are affected by the thickness of the film.<sup>24</sup> Spectra-deconvolution using Gaussian function was carried out in OriginLab 2019 to distinguish overlapping absorptions. A deconvolution was considered successful for a  $R^2$  goodness fit of the deconvolution product higher than 0.98. The fit was achieved by allowing a maximum tolerance of  $\pm 20$  cm<sup>-1</sup> for the wavenumber,  $\pm 30$  for the full width half maximum (FWHM) and allowing only positive



values for the peak area. A set of 9 peaks was utilized in the fingerprint region ( $700\text{--}1300\text{ cm}^{-1}$ ) and their fitting was executed within the specified tolerance margins. These tolerance values were necessary in order to account for the substantial chemical modification of the species caused by changes in the material composition (i.e. enrichment in nitrogen).

Complementary chemical analysis was performed by X-ray Photoelectron Spectroscopy (XPS), performed in a Thermofisher K-alpha system. An Al K-alpha source ( $1486.7\text{ eV}$ ) was used, the analyzer was set in CAE (Constant Analyzer Energy) mode with  $20\text{ eV}$  pass energy. Measurements were taken after a  $30\text{ s}$  etching step using  $\text{Ar}^+$  ions ( $1000\text{ eV}$ ). Surface charges during data acquisition were neutralized with the aid of a low-energy flood gun providing electrons and  $\text{Ar}^+$  ions ( $<5\text{ eV}$ ). The spectra were deconvoluted using CasaXPS<sup>®</sup> to ascertain the environment of the elements. References of silicon carbide ( $\text{SiC}$ ) and nitride ( $\text{Si}_3\text{N}_4$ ) were used to verify Si–C and Si–N bond energies and valence.

#### *Surface morphology, roughness, nanostructure and interface*

The surface roughness of the films was measured in tapping mode with an Agilent Technologies 5500 atomic force microscope (AFM). Scan size and tip details are provided elsewhere.<sup>25</sup> The nanostructure of the film was studied with high-resolution transmission electron microscope (HR-TEM) operating at  $80\text{ kV}$ , as described in a previous work.<sup>23</sup> Nanodiffraction and HR-TEM imaging were used to determine the morphology and the amorphous or crystalline state of the film. Additional chemical information was obtained by scanning transmission electron microscopy-high angle annular dark field (STEM-HAADF) imaging and electron energy loss spectroscopy (EELS). STEM-HAADF images were acquired with a  $68\text{--}174.5\text{ mrad}$  inner-outer collection angle, using a  $0.1\text{ nm}$  probe size. A cross-section of the  $\text{SiO}_x\text{N}_y$  film was prepared by focused ion beam (FIB) method described elsewhere,<sup>23</sup> stored under inert atmosphere and analyzed with minimal delay to reduce contamination.

#### *Functional and mechanical properties*

Nanoindentation tests were carried out on thick films (ca.  $500\text{ nm}$ ) to limit substrate contribution, using an UltraNanoIndenter apparatus (CSM Instruments, Anton Paar) equipped with a Berkovich diamond indenter. A gradually increasing load up to  $0.5\text{ mN}$  was applied, then maintained for  $30\text{ s}$ , and lastly reduced to zero, with  $1\text{ mN}\cdot\text{min}^{-1}$  load/unload rates. Load and displacement resolutions were  $0.25\text{ }\mu\text{N}$  and  $0.1\text{ nm}$ , respectively. Elastic modulus and hardness data were calculated from the load vs. depth curves, utilizing the method proposed by Oliver and Pharr.<sup>26</sup>

Nanoscratch tests were performed using a Nanoscratch Tester (CSM Instrument, Anton Paar) equipped with a spherical diamond indenter ( $2\text{ }\mu\text{m}$  radius). Scratch load, displacement speed and further

details on the nanoscratch tests have been reported in a previous work.<sup>23</sup> Track analysis and determination of the critical normal loads describing the coating adhesive failures were facilitated by the use of an optical microscope (Nanoscratch CSM) and scanning electron microscope (SEM) apparatus (Vega 3 TESCAN). Special attention was given to film delamination from the substrate.

Wettability was measured with a GBX apparatus using  $0.35 \pm 0.01$   $\mu\text{l}$  distilled-water droplets that were carefully placed at five different locations of the sample surface at ambient. The equilibrium static contact angle was measured using a CCD camera.

The wet etching corrosion resistance of the films was assessed using a buffered oxide etchant (BOE) wet etchant, used in microfabrication.<sup>27</sup> It is a 6:1 solution consisting of 6 parts  $\text{NH}_4\text{F}$  (40 wt%) and 1 part HF (49 wt%). The samples were immersed for up to 60 s under continuous stirring at  $25^\circ\text{C}$ . The etching rate ( $\text{\AA}\cdot\text{s}^{-1}$ ) of each  $\text{SiO}_x\text{N}_y$  film was determined by measuring the thickness on ten different locations using SE before and after immersion.

## Results and Discussion

### *SiO<sub>x</sub>N<sub>y</sub> deposition*

It must be noted that the experimental runs TD1 and TD2, which featured a maximum temperature of  $550^\circ\text{C}$  and  $580^\circ\text{C}$  in their respective isothermal region, did not result in any visible  $\text{SiO}_x\text{N}_y$  deposition, well coherent with recent results detailing the decomposition of the TDMSA precursor above  $580^\circ\text{C}$ .<sup>18</sup> Figure 1 presents results of runs TD3, TD6, TD7 and TD8 performed at  $650^\circ\text{C}$ , utilizing the TDMSA- $\text{O}_2$ - $\text{NH}_3$  chemistry. As illustrated in the photograph of Figure 1(a), increasing the temperature to  $650^\circ\text{C}$  through run TD3 proved successful as noted by the iridescence. In these conditions, film formation occurs with a maximum deposition rate (DR) of  $0.92 \text{ nm}\cdot\text{min}^{-1}$  on sample p2 and a maximum nitrogen content of 9.5 at.% on sample p6, as measured by SE. Visual inspection of Figure 1(a) shows that minimum temperature of  $610^\circ\text{C}$  is necessary for film formation, with possible, albeit minimal, deposition between  $585$ – $610^\circ\text{C}$ . No deposition is noted below  $585^\circ\text{C}$ , an observation coherent with the lack of deposition in runs TD1 and TD2. Run TD4, although utilizing a lower precursor flow rate, still resulted in film formation. A maximum DR of  $0.96 \text{ nm}\cdot\text{min}^{-1}$  was noted in the isothermal region, higher than the one noted for TD3, attributed to the higher  $\text{O}_2$ :TDMSA flow ratio (1 in TD4 compared to 0.33 in TD3, Table 1). However, this higher  $\text{O}_2$ :TDMSA ratio decreased the nitrogen content of the  $\text{SiO}_x\text{N}_y$  films to a maximum of 0.7 at.% N, as a result of increased oxidation of the native Si-N bond in the precursor molecule.

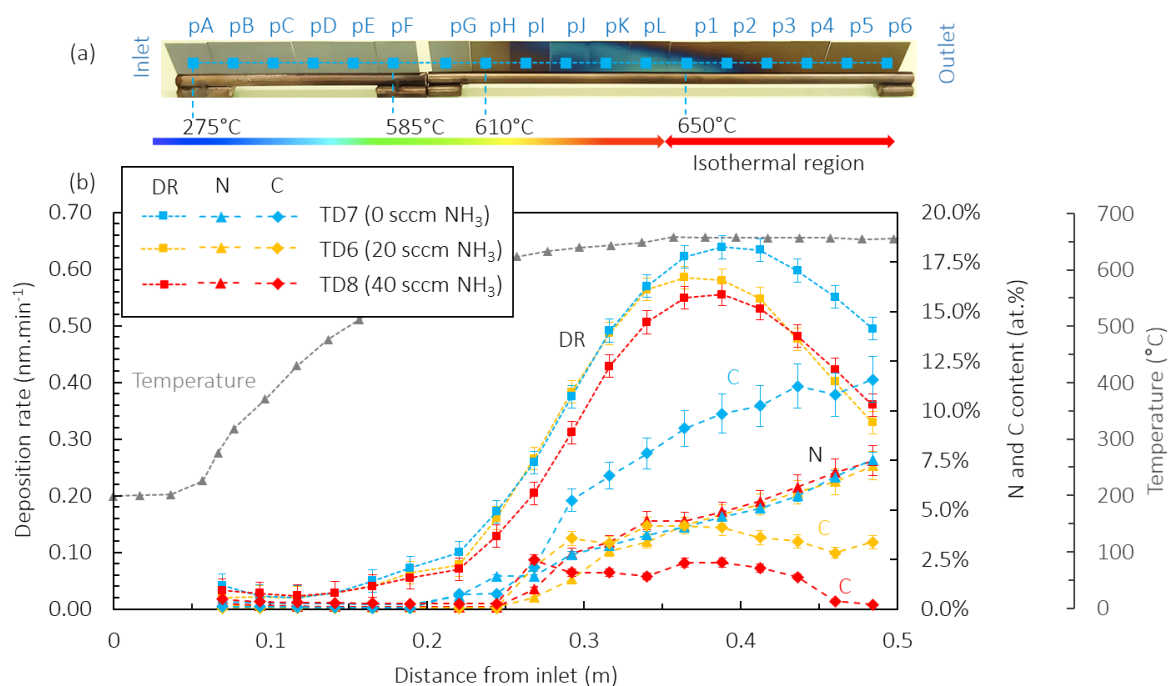


Figure 1. Photograph of Si-sample array after deposition of run TD3 (a) and evolution of the deposition rate (DR, squares), the N (triangles) and C (diamonds) contents, as measured by spectroscopic ellipsometry, for variable  $\text{NH}_3$  flow rate (runs TD6, TD7, TD8) at SPT  $650^\circ\text{C}$ , with the corresponding temperature profile (grey triangles) (b).

Run TD5 was performed in absence of  $\text{O}_2$ , increasing the maximum nitrogen content to 16.5 at.%. The lack of  $\text{O}_2$  supply however resulted in a drastic decrease of the DR, which dropped to values below  $0.2 \text{ nm}\cdot\text{min}^{-1}$ . It is obvious that a trade-off exists between film formation (promoted through higher  $\text{O}_2$  supply) and enrichment of the composition in nitrogen (promoted by lower  $\text{O}_2$  supply). The competitive incorporation between O and N has been encountered in other literature detailing the CVD of silicon oxynitrides.<sup>28-30</sup>

By fixing the TDMSA precursor flow rate at 2 sccm, the  $\text{O}_2$  flow rate was reduced to 0.6 sccm for runs TD6, TD7 and TD8 to revert the  $\text{O}_2$ :TDMSA flow ratio back to ca. 0.3 (Table 1). The  $\text{NH}_3$  flow rate was varied between 0–40 sccm across these runs. Figure 1(b) presents the evolution of the average DR and film content in N and C along the reaction chamber for runs TD6, TD7 and TD8. Deposition is initiated at  $\sim 510^\circ\text{C}$ , albeit with a notably low DR of ca.  $0.05 \text{ nm}\cdot\text{min}^{-1}$  for all three runs and in absence of nitrogen in the films. Incorporation of nitrogen is encountered only on films for which the local temperature exceeds  $610^\circ\text{C}$ . A maximum DR of  $0.64 \text{ nm}\cdot\text{min}^{-1}$  is achieved in the isothermal region ( $650^\circ\text{C}$ ) for TD7, decreasing slightly to 0.59 and  $0.55 \text{ nm}\cdot\text{min}^{-1}$  with  $\text{NH}_3$  flow rate increase from 20 to 40 sccm in TD6 and TD8, respectively.

The utilization of the BEMA SE model provides additional information on the TD6, TD7 and TD8 films composition. Nitrogen is first encountered at 0.22 m from the inlet and presents a continuous increase. Interestingly, although film formation decelerates beyond the maximum DR, the nitrogen content of the material increases, reaching ca. 7.5 at.% on the final sample of the array (p6) for all three runs. Given that the temperature is constant in the isothermal region, the decrease of the DR in the 0.36–0.50 m range is accredited to the O<sub>2</sub> consumption in the gas phase. Consumption of the TDMSA precursor was excluded given its detection in the effluent gases of all three runs, in similar quantities.<sup>18</sup> Considering the aforementioned competition between oxygen and nitrogen, the continuous increase of the N content in this region (0.36–0.50 m) is logical.

For the tested conditions however, variation of the NH<sub>3</sub> supply did not aid in increasing the N composition. The nitrogen profiles remained almost identical across the three runs (Figure 1(b)). Moreover, nitrogen was probed even in absence of NH<sub>3</sub> (TD7). These results demonstrate the role of the TDMSA precursor as a dual Si and N source. The most significant contribution of NH<sub>3</sub> is a decrease in carbon incorporation.<sup>31, 32</sup> A maximum carbon concentration of 11.6 at.% is measured for TD7, dropping to values below 2.3 at.% for the higher NH<sub>3</sub> supply used in run TD8.

Globally, the refractive index of the films ranges from 1.465 to 1.621. The extinction coefficient of the SiO<sub>x</sub>N<sub>y</sub> films is zero independent of the deposition conditions, allowing their application in multi-layer anti-reflective coatings (ARC).<sup>33</sup>

A similar parametric analysis based on the variation of the O<sub>2</sub> flow rate in absence of NH<sub>3</sub> (runs TD7, TD11, TD12 and TD14) has been reported elsewhere.<sup>19</sup> In that report, the extracted compositional and thickness characteristics of all 18 samples from these runs have been utilized for the development of a kinetic model for the computational fluid dynamics simulation of SiO<sub>x</sub>N<sub>y</sub> deposition.

### *Composition trends*

Figure 2 presents the film composition in Si, O, N, C and H, as obtained from ion beam analyses (IBA), for runs TD6 to TD14. Sample p2 was analyzed for all runs, targeting a minimum film thickness of 80–100 nm required for IBA.

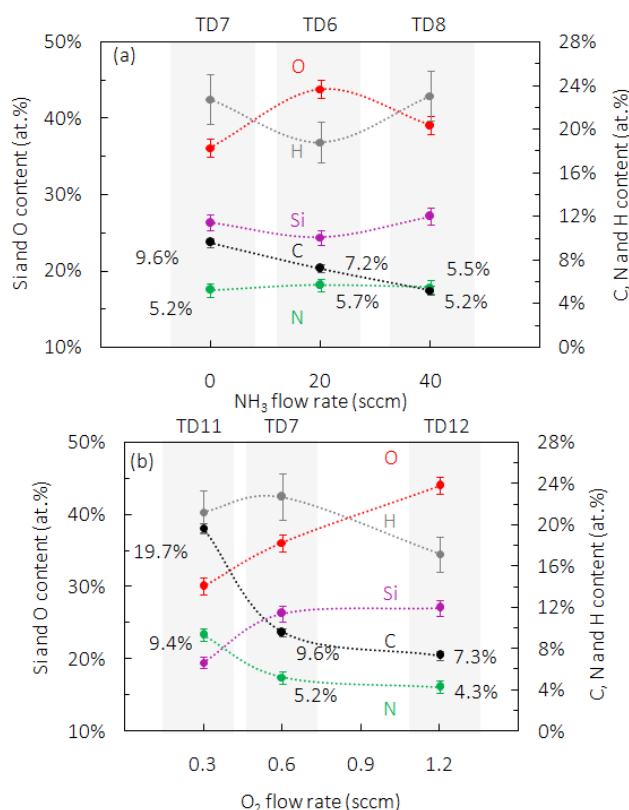


Figure 2. Ion beam analysis composition results for films produced under varying  $\text{NH}_3$  (a) and  $\text{O}_2$  (b) flow rates.

The effect of the variable  $\text{NH}_3$  flow rate (runs TD6 to TD8) on the film composition is presented in Figure 2(a). The trends previously noted by SE are reproduced. First, the minimal role of  $\text{NH}_3$  on the nitrogen content is once more encountered in the IBA results, varying insignificantly between 5.2 and 5.7 at.%. Nitrogen is probed even for 0 sccm  $\text{NH}_3$  (TD7), confirming that it originates from TDMSA precursor. Carbon is also found in the films, ranging between 5.2 and 9.6 at.%, originating from the organic  $-\text{CH}_3$  moieties of TDMSA.  $\text{NH}_3$  effectively cleaves the methyl ligands of the precursor, presenting a linear reduction in carbon incorporation as the  $\text{NH}_3$  flow rate increases. In addition, hydrogen concentrations spanning 18.8–23.1 at.% H are probed in the films. No specific correlation between  $\text{NH}_3$  flow rate and hydrogen content is revealed. Interestingly however, the H concentration follows a trend similar to that of Si and reverse compared to O.

The effect of the  $\text{O}_2$  flow rate (runs TD7, TD11, TD12) on the film composition measured by IBA is shown in Figure 2(b). IBA confirms the competitive incorporation of O and N, as previously noted by SE. Considering the higher electronegativity of O atoms to N, the presence of higher oxygen concentration in the gas phase facilitates O substituting N towards Si–O–Si bridge-formation in the lattice. Thus, an increase in  $\text{O}_2$  supply results in higher oxygen content in the films, accompanied by lower nitrogen incorporation that is noted to drop from 9.4 at.% N for 0.3 sccm  $\text{O}_2$  to 4.3 at.% N for 1.2

sccm O<sub>2</sub>. It is noted that the O/(O+N) relative atomic concentration has been characterized as a crucial factor that influences the chemical bonding configuration and physical properties of the film.<sup>10</sup> Chen et al. proposed that when the O/(O+N) ratio is above 0.4, nitride-like structures in the film are transformed and lean towards oxide-like structures. In consequence, the electronic properties change when the SiO<sub>x</sub>N<sub>y</sub> layer is intended for gate dielectric applications.<sup>34</sup> In the present work, all films exhibit O/(O+N) ratios between 0.75–0.9, clearly showing a more oxide-like structure.

Carbon incorporation also decreases for higher O<sub>2</sub> supply, being reduced from 19.7 at.% at 0.3 sccm O<sub>2</sub> to 7.3 at.% at 1.2 sccm O<sub>2</sub>. In terms of hydrogen content, the IBA results reveal concentrations varying non-monotonously from 17.2–22.7 at.% H, with lower levels of H observed for 1.2 sccm O<sub>2</sub>. In view of the composition trends, it is concluded that the evolution of the hydrogen content is complex, due to the multiple forms it can be incorporated as: N–H, –CH<sub>x</sub>, adsorbed H<sub>2</sub>O, Si–OH terminal group and potential Si–H. Evidence for the presence of such bonding states relies on infrared analysis, as presented in the next section.

Lastly, changes in film composition due to the modification of the deposition temperature (TD7, TD14) are shown in Figure SI2. Although a trend is difficult to conclude with only two datasets, N incorporation is noted to increase from 4.2 to 5.2 at.% N when the temperature is raised from 625°C to 650°C. A co-deposition of C and N through a common intermediate species could be supposed, given the parallel increase in carbon content. The more prominent increase of hydrogen content could also support the assumption that most H in the films is inserted through N–H and/or –CH<sub>x</sub> moieties.

### *Chemical bonding and nanostructure*

#### **FT-IR**

Figure 3 explores the FT-IR chemical bonding in SiO<sub>x</sub>N<sub>y</sub> films. A representative spectrum of sample p1, taken from the isothermal region of run TD7 is shown in Figure 3(a). Multiple absorptions are identified. The characteristic transverse optical TO1, TO2 and TO3 modes corresponding respectively to the rocking, bending and symmetric stretching vibrational modes of the Si–O–Si bond are noted, along with the TO3-LO3 pair observed after application of a 60° oblique incidence angle.<sup>35, 36</sup> Absorptions relating to organic carbon incorporation, e.g. the bending vibration of CH<sub>3</sub> in Si-(CH<sub>3</sub>)<sub>x</sub> groups at ca. 1270 cm<sup>-1</sup>, are also observed, their origin being the incompletely decomposed –CH<sub>3</sub> groups in the TDMSA precursor molecule. In addition, an absorption at ca. 936 cm<sup>-1</sup> is identified, corresponding to the stretching vibration of Si–N.<sup>37, 38</sup> Furthermore, additional nitrogen-related absorptions are noted at approximately 470 and 840 cm<sup>-1</sup>, corresponding to the symmetric and asymmetric stretching modes of the Si–N bond, respectively.<sup>39</sup> At higher frequencies, the N–H stretching vibration is noted at around 3400 cm<sup>-1</sup>,<sup>37</sup> presenting an asymmetry caused by a “tail” that extends towards lower wavenumbers (ca.

3300  $\text{cm}^{-1}$ ), attributed to hydrogen bonds between hydrogen and the lone electron pairs of nearby nitrogen atoms.<sup>40</sup> A summary of all encountered absorptions is listed in Table SII of *Supporting Information*. A Si–OH absorption at ca. 3650  $\text{cm}^{-1}$  and organic –CH<sub>3</sub> asymmetric stretching absorptions appearing as small shoulders at ca. 2900  $\text{cm}^{-1}$  are noted in the band as well.<sup>41</sup> In light of the FT-IR results of Figure 3(a), the bonding types of C and H are –CH<sub>x</sub>, Si–OH, physisorbed H<sub>2</sub>O and N–H. As a result, the non-monotonous evolution of the hydrogen content revealed by IBA in Figure 2(a) and (b) is explained by its distribution across these various hydrated species

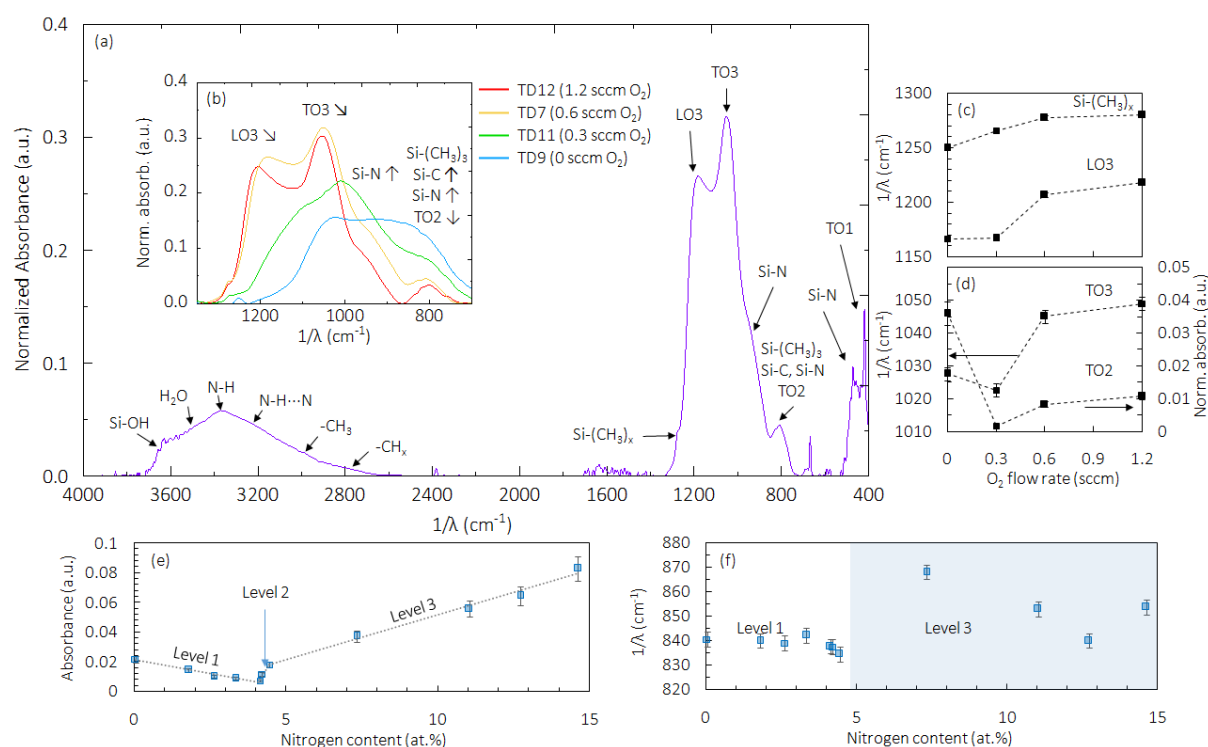


Figure 3. FT-IR analysis. Survey spectrum of the p1 SiO<sub>x</sub>N<sub>y</sub> sample from run TD7, analyzed at 60° incidence angle (a). Evolution of the fingerprint region as a function of the O<sub>2</sub> flow rate (b). Evolution of Si–(CH<sub>3</sub>)<sub>x</sub> and LO3 positions (c), TO3 position and TO2 intensity (d) as a function of the O<sub>2</sub> flow rate. Evolution of the intensity (e) and position (f) of the absorption probed between 830–870  $\text{cm}^{-1}$  for SiO<sub>x</sub>N<sub>y</sub> samples produced under various conditions, as a function of their nitrogen content.

An evolution of the fingerprint region (700–1300  $\text{cm}^{-1}$ ) as a function of the O<sub>2</sub> flow rate, analyzed for an incidence angle of 60° by probing sample p1, is presented in Figure 3(b). Multiple conjoining absorptions impede a straightforward analysis, though general trends are noted. The evolution of these trends is indicated by arrows illustrating the position shift and change in intensity of the main peaks. For example, the downwards arrow pointing to the right for the LO3 absorption is



signifying a decrease in intensity, alongside a shift towards lower wavenumbers. As revealed by IBA in Figure 2(b), a reduction in O<sub>2</sub> supply from 1.2 sccm (TD12) to 0 sccm (TD9) results in films with higher nitrogen and carbon incorporation. This is reflected in the FT-IR spectra through a reduction of the LO3 and TO3, with parallel increase of the Si–N and Si–C absorbance (Figure 3(b)). The LO3-TO3 pair is no more observable at 0.3 and 0 sccm O<sub>2</sub>, and the overall spectrum appears as if “shifting” towards lower wavenumbers.

Due to the spectral complexity, deconvolution is applied to aid with the identification of individual absorptions and positions. The considered absorptions, as well as an example of deconvolution of the fingerprint region, are presented in Figure SI3 of *Supporting Information*. The evolution of selected absorptions after deconvolution is presented in Figures 3(c) and 3(d) as a function of the O<sub>2</sub> flow rate (runs TD7, TD9, TD11 and TD12). Notably, the position of the Si–(CH<sub>3</sub>)<sub>x</sub> absorption is shown to shift towards higher wavenumbers with increasing O<sub>2</sub> flow rate (Figure 3(c)), indicating the addition of more O atoms to the Si–(CH<sub>3</sub>)<sub>x</sub> complex.<sup>42</sup> With O atoms being more electronegative, addition of more O atoms in the environment surrounding the Si atom of the Si–(CH<sub>3</sub>)<sub>x</sub> complex attracts the bonding electrons towards O. This in turn shortens the Si–(CH<sub>3</sub>) bond length, resulting in the Si–(CH<sub>3</sub>)<sub>x</sub> complex vibrating at higher frequencies. Similarly, the LO3 mode for runs at higher O<sub>2</sub> flow rates also shifts towards higher frequencies, an effect that hints again at more oxygen-rich films, as confirmed by IBA results (Figure 2(b)). When the O<sub>2</sub> supply is low (0.3 sccm) however, the LO3 position shifts substantially from the anticipated ~1250 cm<sup>-1</sup> down to 1170 cm<sup>-1</sup>. It is proposed that a different vibration absorbs at the 1170 cm<sup>-1</sup> frequency, and that the LO3 is absent. Referring to Table SI1, this absorption could be associated to the TO4-LO4 pair.<sup>37, 43</sup>

TO3 behaves similarly, shifting from ca. 1050 cm<sup>-1</sup> at 1.2 sccm O<sub>2</sub> to lower wavenumbers as the oxygen supply is decreased (Figure 3(d)). The lowest position noted for TO3 is 1022 cm<sup>-1</sup>. Given that the Si–CH<sub>2</sub>–Si stretching vibration absorbs at 1000–1020 cm<sup>-1</sup>,<sup>29, 44</sup> it is likely that the absorption noted at this wavenumber might be assigned to the Si–CH<sub>2</sub>–Si bond instead of the typical Si–O–Si TO3 mode when low O<sub>2</sub> flow rates are supplied. Similar discussion can be made for the 800–820 cm<sup>-1</sup> peak (Figure 3(d)). Both Si–C and Si–O (TO2) absorb in this range.<sup>45, 46</sup> A high absorbance is noted at 0 sccm O<sub>2</sub>, decreasing once O<sub>2</sub> is added to the inlet gas composition, then increasing again for higher O<sub>2</sub> flow rates. This is likely linked to decreasing absorption of Si–C bonds with parallel increase of the Si–O TO2 mode. Therefore, we propose that for low O<sub>2</sub> flow rates, and by extension low film composition in O, a disappearance of the LO3-TO3 pair (Figure 3(b)) results in carbon-related counterparts absorbing at wavenumbers that are classically attributed to Si–O absorptions, i.e. Si–CH<sub>2</sub>–Si instead of TO3, and Si–C instead of TO2.

The evolution of the intensity of the absorption found at ca. 850 cm<sup>-1</sup> is shown in Figure 3(e), plotted as a function of the nitrogen content. The graph contains results of deconvolution analyses



carried out on FT-IR spectra from samples produced under various conditions, at different positions in the reactor, and from both TDMSA-O<sub>2</sub>-NH<sub>3</sub> and TDMSA-O<sub>2</sub> chemistries. The bonds attributed to this absorption are the rocking of CH<sub>3</sub> vibrations in Si-(CH<sub>3</sub>)<sub>3</sub> groups<sup>47</sup> or the Si-N asymmetric stretching vibrational mode.<sup>39</sup> Despite the variety of the samples, three regions with almost linear evolutions can be distinguished, seemingly being dependent entirely on the nitrogen content. The first region (Level 1) is found between 0.0 and 4.0 at.% N, followed by a short region (Level 2) at 4.0–4.5 at.% N. Lastly, a region beyond 5.0 at.% N (Level 3) is encountered. The evolution of the 840–870 cm<sup>-1</sup> absorption at each level, although monotonous, follows different slopes, decreasing at Level 1, then increasing for Levels 2 and 3. Given this behavior and the overlap of the Si-(CH<sub>3</sub>)<sub>3</sub> and Si-N asymmetric stretching absorptions at this wavenumber, we suppose that for Level 1, namely for samples with <4.0 at.% N, the probed signal corresponds to a Si-(CH<sub>3</sub>)<sub>3</sub> absorption. As the nitrogen content increases, these vibrations decrease as a result of more Si atoms being connected to N. For Levels 2 and 3 (4.0–4.5 and >5.0 at.% N), the absorption is most likely connected to the appearance of the Si-N asymmetric stretching vibrational mode, in good coherence with the increase in nitrogen content in the films.

The evolution of the position of this particular absorption is presented in Figure 3(f) as a function of the nitrogen content of each sample. For the previously defined Level 1 (<4.0 at.% N), the absorption is probed at ca. 840 cm<sup>-1</sup>, corresponding well to the position of the rocking vibration of CH<sub>3</sub> in Si-(CH<sub>3</sub>)<sub>3</sub> groups.<sup>47</sup> The wavenumber decreases down to 834 cm<sup>-1</sup> for Level 2 (4.0–4.5 at.% N), with the vibration at lower frequencies indicating a lengthening of the bond between the atoms in question. The lengthening may be assigned to the replacement of electronegative atoms (O) in the surrounding network by atoms with lower electronegativity (N). It is likely that the bond absorbing at Level 2 is still the rocking vibration of CH<sub>3</sub> in a Si-(CH<sub>3</sub>)<sub>3</sub> complex, that is most likely transitioning towards a Si-(CH<sub>3</sub>)<sub>x</sub> complex. At Level 3 (>5 at.% N), the position shifts substantially to 870 cm<sup>-1</sup>, in good correlation with the appearance of the asymmetric stretching vibration of the Si-N bond, noted between ca 880 and 840 cm<sup>-1</sup> in the literature.<sup>48</sup> The shift of this absorption towards lower wavenumbers, similarly to the one observed between 7 and 13 at.% N (Figure 3(f)), has been associated with a decreasing N-H concentration.<sup>49</sup> The higher wavenumber (855 cm<sup>-1</sup>) noted for 14.6 at.% is potentially linked to deposition conditions.

It is noted that the Si-N asymmetric stretching absorption has been described as an indicator of the binding state in a SiO<sub>x</sub>N<sub>y</sub> network. Two types of local structures are suggested by Behrens et al.,<sup>48</sup> i.e. a random mixture model (RMM) and a random binding model (RBM). RMM is defined as a mixture of randomly distributed SiO<sub>2</sub> and Si<sub>3</sub>N<sub>4</sub> phases, resulting macroscopically in an amorphous SiO<sub>x</sub>N<sub>y</sub> network. In RBM on the other hand, “the bonds between Si, O and N constitute a fourfold coordination and represent a homogeneous O-Si-N network in five different tetrahedral configurations of SiO<sub>v</sub>N<sub>4-v</sub>, where v=0–4”, as per Behrens et al. and Shahpanah et al.<sup>9, 48</sup> Multiple authors have linked the presence of this asymmetric stretching Si–N absorption to Si<sub>3</sub>N<sub>4</sub>, and by extension to the RMM model.<sup>50, 51</sup>

## XPS

For samples presenting high carbon content (e.g. runs TD9 and TD11), the distinction between the Si-C and TO2 absorptions at  $800\text{ cm}^{-1}$  by FT-IR analysis is not easily discernible. The two absorptions are oftentimes found to overlap, as is the case for the p1 sample of run TD11 with 20.1 at.% C, the FT-IR spectrum and deconvolution of which are shown in Figure SI4 of *Supporting Information*. To help better ascertain the presence of carbon incorporation as carbidic Si-C and the overall chemical environment of the elements, high resolution XPS spectra were considered.

Figure 4 presents XPS Si 2p, N 1s and C 1s spectra for p6  $\text{SiO}_x\text{N}_y$  samples produced under varying  $\text{O}_2$  flow rates (runs TD7, TD9, TD11 and TD12) and their deconvolution based on literature data.<sup>52–54</sup> A summary of the atomic concentrations obtained by integration of each binding energy peak is found in Table SI2 of *Supporting Information*. It is noted that the electron configuration gives information on the composition and the bonding state of atoms, which can effectively evolve and change based on the applied process conditions. For high  $\text{O}_2$  flow rate, as is the case for the TD12 film (1.2 sccm  $\text{O}_2$ ), the Si 2p spectrum (Figure 4(d)) is deconvoluted into four sub-contributions with binding energies of 103.3, 102.6, 101.2 and 100.3 eV, corresponding to  $\text{Si}(\text{O})_4$ , O-N-Si-O,  $\text{Si-N}_x$  or  $\text{C}_n\text{SiN}_{4-n}$ , and Si-Si-C, respectively. The last two components have minimal concentrations for TD12 conditions. The mixed environment of Si is mostly dominated by N and C for TD11 and TD9 conditions (Figure 4(b) and (a)), then by O at TD12 and TD7 conditions (Figure 4(d) and (c)). The 102.6 eV O-N-Si-O component is showing the highest intensity for TD12 and TD7, corresponding to Si-O bonding in nitride films,<sup>55</sup> coherent with the deposition of a  $\text{SiO}_x\text{N}_y$  film. Upon closer inspection of the TD11 and TD9 Si 2p spectra, a shift towards 102.0 eV is noted for O-N-Si-O. This shift in the binding energy of photoelectron peaks is encountered when the valence state of the bonding atoms changes, namely a multiphase configuration shift from N-Si-O<sub>3</sub> (103.0 eV), to N<sub>2</sub>-Si-O<sub>2</sub> (102.8 eV) and to N<sub>3</sub>-Si-O (102.2 eV).<sup>56</sup> The XPS results further underline the transition from a RMM state ( $\text{O}_x\text{-Si-N}_y$ ) to RBM (distinction of Si-N<sub>x</sub> rich configuration), as revealed by FT-IR.

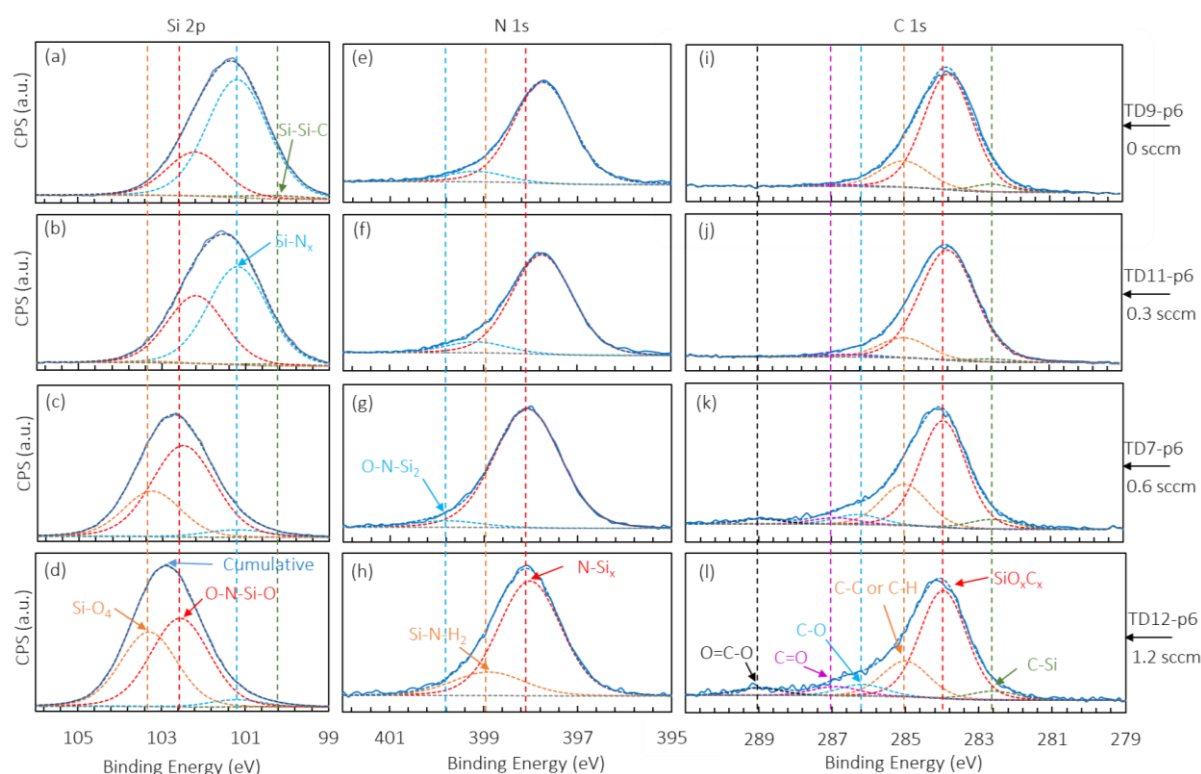


Figure 4. Si 2p (spectra a, b, c and d), N 1s (spectra e, f, g and h) and C 1s (spectra i, j, k and l) XPS spectra of  $\text{SiO}_x\text{N}_y$  p6 samples produced under variable  $\text{O}_2$  flow rate mentioned on the right (runs, TD7, TD9, TD11, TD12).

The second most prominent component for TD12 and TD7 conditions corresponds to a tetrahedral configuration of  $\text{Si}(\text{O})_4$  (103.3 and 103.1 eV, respectively), describing the silica character of the films.<sup>10</sup> This component however disappears for TD11 and TD9 (Figure 4(b) and (a)), similar to the decrease of the Si-O-Si LO3, TO3, TO2 absorptions observed by FT-IR. Correlating these two, it could be proposed that tetrahedral configurations, in which a silicon atom is uniquely bonded to oxygen, do not exist in the films for TD11 and TD9 conditions, leading to the decrease (or even disappearance) of the Si-O-Si TO3, LO3 and TO2 infrared absorptions.

The component with binding energy of 101.0 eV can indicate the presence of  $\text{C}_n\text{SiN}_{4-n}$  polysubstituted tetrahedrons,<sup>57</sup> yet is more likely related to the Si- $\text{N}_x$  component that emerges with high atomic concentrations for TD11 and TD9 (Figure 4(b) and (a)), in between stoichiometric  $\text{Si}_3\text{N}_4$  (101.9 eV)<sup>55</sup> and  $\text{Si-Si}_2\text{-O-N}$  (101.2 eV).<sup>56</sup> The final component with a binding energy of 100.3 eV is attributed to Si-Si-C or  $\text{Si-O}_1\text{-C}_3$ .<sup>53</sup> No low energy component near 99.0–99.6 eV ( $\text{Si}(\text{Si})_4$ ) was detected, testifying the absence of Si clusters in the samples and confirming the amorphous state.<sup>56</sup>

The N 1s spectrum obtained for TD12 conditions (Figure 4(h)) is deconvoluted into a primary peak (398.0 eV), intermediate to N-Si<sub>3</sub> (397.4–398.4 eV) and Si<sub>2</sub>-N-H (398.0 eV).<sup>58</sup> The observed binding energy hints at a predominant surrounding of N by Si (N-Si<sub>x</sub>) evidencing the deposition of a nitride-type material, non-excluding the presence of N-H bonds. This binding energy shifts towards 397.7 eV as the O<sub>2</sub> flow rate is decreases (Figure 4(f) and (e)), evidencing a loss in N-H bonds and increasing N-Si<sub>3</sub> bonding peak.<sup>58</sup> This is coherent with the transition towards a RMM state revealed by the FT-IR results. A second component attributed to Si-N-H<sub>2</sub> groups is probed with a binding energy of 398.9 eV.<sup>58</sup> This binding state is unique to TD12 and is not probed for the other runs. Instead, the emergence of a component at 399.8 eV is noted for TD7 (Figure 4(g)), corresponding to a mixed nitride-oxide environment with a O-N-Si<sub>2</sub> bonding scheme.<sup>58</sup> As the O<sub>2</sub> flow rate decreases for TD11 and TD9 (Figure 4(f) and (e)), its position shifts to 399.2 eV, likely linked to an aliphatic C-NH<sub>2</sub> amine.

The C 1s XPS spectrum obtained for TD12 conditions (Figure 4(i)) is deconvoluted into 6 subpeaks, measuring binding energies of 289.0, 286.9, 286.3, 285.0, 284.0 and 282.6 eV, corresponding to O=C-O, C=O, C-O, C-C/C-H, SiO<sub>x</sub>C<sub>x</sub> with  $x \approx 2$  or C<sub>n</sub>SiN<sub>4-n</sub>, and C-Si, respectively.<sup>52, 53</sup> If present, a C(sp<sup>2</sup>)-N environment could contribute to the peak at 286.3 eV.<sup>57</sup> A small percentage of Si-C is also probed. However, only up to 5 % of the incorporated carbon is found in a Si-C-Si environment. Correlating this back to the FT-IR results (Figure 3(d)), it could be proposed that the peak probed at ca. 1020 cm<sup>-1</sup> under low O<sub>2</sub> flow rates (TD9, TD11) should be attributed to mixed Si-O-Si TO3 and Si-CH<sub>2</sub>-Si absorptions. Similarly, the peak at ca. 800 cm<sup>-1</sup> is very likely a mixed TO2/Si-C absorption.

Globally, the increased O<sub>2</sub> supply is reflected in the higher oxygen content of films as seen in the atomic concentrations of Table SI2 (13.54 at.% for TD9, 0 sccm O<sub>2</sub>, increasing to 49.69 at.% for TD12, 1.2 sccm O<sub>2</sub>). The evolution of all elements are coherent with IBA results. The environment of Si appears to be changing substantially as a function of the O<sub>2</sub> supply. At the highest O<sub>2</sub> flow rates, Si is involved primarily in Si-O<sub>4</sub> and O-N-Si-O configurations. Overall, the XPS measurements verify the presence of a N<sub>x</sub>-Si-O<sub>y</sub> bonding complex in the amorphous SiO<sub>x</sub>N<sub>y</sub> films through formation of individual Si-O and Si-N bonds. It is noted that the cumulative Si 2p peak position shifts from ca. 103.1 to 101.4 eV with decreasing O<sub>2</sub> flow rate, notably starting close to the SiO<sub>2</sub> binding energy (103.4 eV) and ending up near the Si<sub>3</sub>N<sub>4</sub> binding energy (101.9 eV).<sup>56</sup>

## TEM

To ascertain the structure of the deposited films, high-resolution TEM has been carried out, shown in Figure 5, for a 500 nm thick film with ca. 6 at.% N, deposited in the isothermal region of run TD10. The high-resolution cross section of Figure 5(a) illustrates the amorphous SiO<sub>x</sub>N<sub>y</sub> film in contact with the [011] oriented monocrystalline Si substrate. A profile of nanodiffraction patterns has been collected along the depth of the film, spaced of 60 nm apart and probing an area of approximately 110

nm<sup>2</sup>. All the diffraction patterns (i.e. at the surface, interface and core of the film), are similar to the one of Figure 5(b), and reveal no diffraction spots, therefore confirming the amorphous nature of the film, independently of the probed depth.

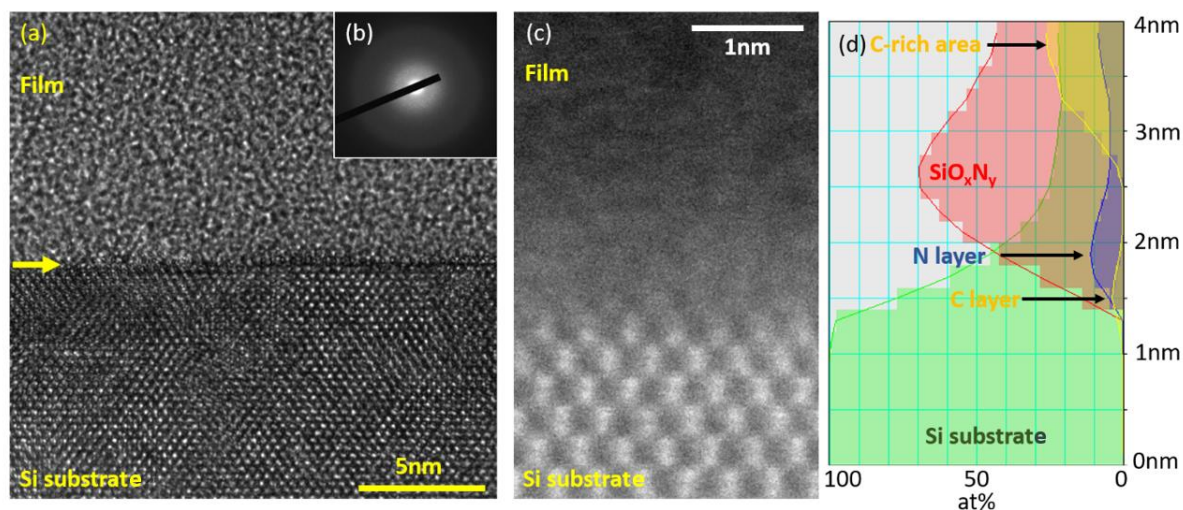


Figure 5. High resolution TEM image of the film-substrate interface (a). Nanodiffraction pattern taken from the core of the SiO<sub>x</sub>N<sub>y</sub> film (b). STEM-HAADF image of the interface (c). Elemental composition profile obtained from EELS Spectrum-Imaging (Si in green, C in yellow, N in blue and O in red) and where the 5 different domains determined by PCA decomposition are specified (d).

The zoom at the interface in Figure 5(a) reveals a porosity-free, intimate and regular contact between substrate and film. The interface is also easily observable through Z-contrast imaging in STEM-HAADF mode at the atomic scale in Figure 5(c). The Si-substrate being heavier compared to the SiO<sub>x</sub>N<sub>y</sub> film, it appears brighter. It is noted that the Si/film interface region constitutes a critical factor for the photoelectronic properties of luminescent silicon and consequently the performance in electronic and optical devices. According to Daldosso et al., a sharp and stable Si/SiO<sub>2</sub> interface provides passivation of non-radiative defect states on the surface, aiding in stable light emission.<sup>59</sup> In order to ascertain the particular binding configuration, i.e. RMM or RBM, a Principal Components Analysis (PCA) decomposition is carried out on the EELS Spectrum-Imaging data after denoising, using the Multivariate Statistical Analysis (MSA) program in the GMS 3.4 Gatan software. This process allows highlighting different components represented by maps (Figure SI5 of *Supporting Information*). Coupling this purely mathematical treatment with the elemental compositions (Figure 5(d)) reveals the complexity of the interface with the presence of 5 different domains. First, the Si-substrate is noted, followed by a carbon-rich layer (C layer), a nitrogen-rich layer (N layer) and a SiO<sub>x</sub>N<sub>y</sub> layer with carbon-enriched domains

(C-rich area). These variations of compositions occur over a very small thickness, around 2 nm, representing the first 3 min of the deposition process during which equilibrium may not have been reached yet. Globally through the film, the matrix seems to contain all the elements, indicating a varying  $\text{SiO}_x\text{N}_y\text{C}_z$  composition, without the presence of separate  $\text{SiO}_2$  and  $\text{Si}_3\text{N}_4$  phases. The film is generally amorphous and adheres to the RBM model, with simultaneous presence of Si-O and Si-N towards a homogeneously distributed  $\text{N}_x\text{-Si-O}_{4-x}$  fourfold coordination.

### *Mechanical and functional properties*

#### **Mechanical properties**

Figure 6 presents the mechanical properties of  $\text{SiO}_x\text{N}_y$  films as a function of the nitrogen content. Samples from the isothermal region of run TD10 have been analyzed for assessment of the elastic modulus  $E$  and hardness  $H$ . Since the temperature in this region was constant and film thickness measured ca. 550 nm, any change in these values can be safely attributed to an evolution of the local film composition and, by extension, the network structure.

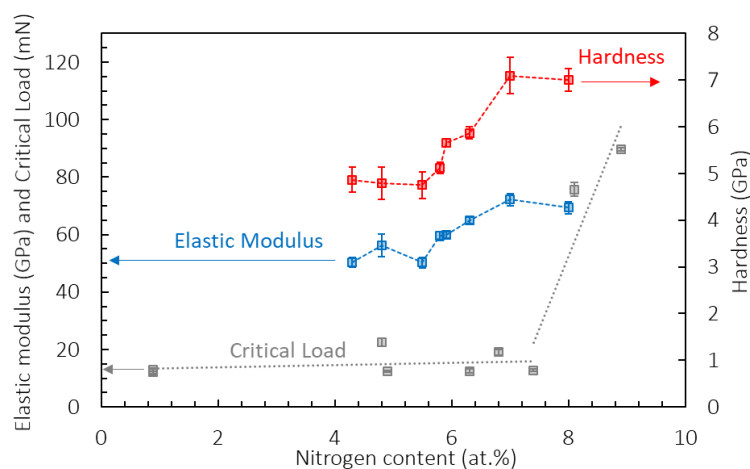


Figure 6. Mechanical properties of films deposited from TDMSA as a function of the nitrogen content. Elastic modulus and Hardness of various samples taken from the isothermal region of run TD10. Nanoscratch critical load results were obtained from p1 samples of various runs. Trend lines added for visual aid.

Both  $H$  and  $E$  are noted to evolve in a similar manner, exhibiting a slightly increasing trend for higher nitrogen incorporation. Based on the previously discussed levels of nitrogen incorporation (Figure 3(e)), this evolution can be divided in three regions. Samples with up to 5.5 at.% N exhibit an



average hardness and elastic modulus of 4.8 and 53 GPa, respectively. The second region is noted between 5.5 and 7 at.% N, in which the  $H$  and  $E$  values are observed to increase with the enrichment of the films in nitrogen. A third region could be defined for samples with a composition above 7 at.% N, for which the  $H$  and  $E$  values appear to stabilize at ca. 7.0 and 70 GPa, respectively. The results illustrate how the partial and progressive replacement of O atoms by N prompts a change in the material network and density despite the constant deposition temperature, which as a result enhances the mechanical properties. The values of  $H$  and  $E$  have been noted to increase with increasing nitrogen contents in the literature as well.<sup>60</sup> It is also recalled that a potential decrease of N-H concentration in the films, based on the discussion of Figure 3(e) and (f), replaced by the creation of additional N-Si bonds in the material network, might also be contributing to the gradual increase of the mechanical properties in the films. In general, both  $E$  and  $H$  measure comparably to values obtained from PECVD  $\text{SiO}_x\text{N}_y$  films containing ca. 10 at.% N, reported at 78.9 and 7.8 GPa, respectively.<sup>61</sup>

The critical load, namely the load required for achieving complete delamination of a film from its substrate, is also shown in Figure 6. Critical load values for films produced from various runs are presented as a function of their nitrogen content. The films exhibit good adhesion to the Si substrate, with critical load values ranging between 12.2 and 22.5 mN, for compositions up to 7 at.% N. Beyond 7 at.% N, the resistance to delamination increases drastically to 89.7 mN. This increased adhesion can be attributed to the enrichment of the films in nitrogen and subsequent increase of N-Si bonds between deposited material and substrate and to the increased film mechanical properties. Recalling Figure 5(d), the EELS elemental composition profile of the sample (ca. 6 at.% N) exhibited indeed a prominent  $\text{SiO}_x\text{N}_y$  presence at the interface, alongside N-rich areas. Localized and/or partial delamination may be observed for low values of load, as shown in Figure SI6 of *Supporting Information*. These local phenomena were however observed rarely, and did not appear systematically.

### Wettability

Water wettability measurements on  $\text{SiO}_x\text{N}_y$  films from various runs are presented in Figure 7. Water contact angle (WCA) values range from 76.9–89.4° and seem to be independent of the nitrogen content (Figure 7(a)). Trevino et al.<sup>62</sup> reported similar values (73.6°) for a thermally grown  $\text{SiO}_x\text{N}_y$  surface with 14.5 at.% N and 14.4 at.% C. No clear correlation was noted when plotting WCA values as versus the carbon and hydrogen contents. Given this non-linear behavior, a multi-factorial dependency of the WCA can be supposed. Such factors can be the overall film composition and surface termination, the roughness and/or surface energy. In the case of silicon nitride materials, surface termination is affected by  $-\text{OH}$ ,  $-\text{NH}_2$  and  $-\text{CH}_3$  groups, with respective contact angles of 42°, 53° and 75° being reported.<sup>63</sup> It is also worth recalling the reduction in wettability for Si-H terminated surface compared to Si-OH.<sup>64</sup> Similarly, replacement of NH or  $\text{NH}_2$  surface bonds by the less polar Si-H

increases the WCA of  $\text{Si}_3\text{N}_4$  films.<sup>65</sup> For oxynitride materials, WCAs spanning at  $98\text{--}110^\circ$  were noted by Zhang et al. for  $\text{SiO}_x\text{N}_y$  coatings with high Si–H content.<sup>66</sup> Based on the above, the measured WCA values are plotted as a function of the intensity of the Si–H wagging or rocking vibrational mode. Although this particular bond absorbs very weakly at  $630\text{--}650\text{ cm}^{-1}$  for the films produced in this work, plotting of the WCA values yields an almost linear trend (Figure 7(a)). This result should be consolidated with dedicated, on purpose experiments. It is also noted that the trend line does not pass through the origin of the coordinate axes, presenting an intercept value of  $76.9^\circ$ .

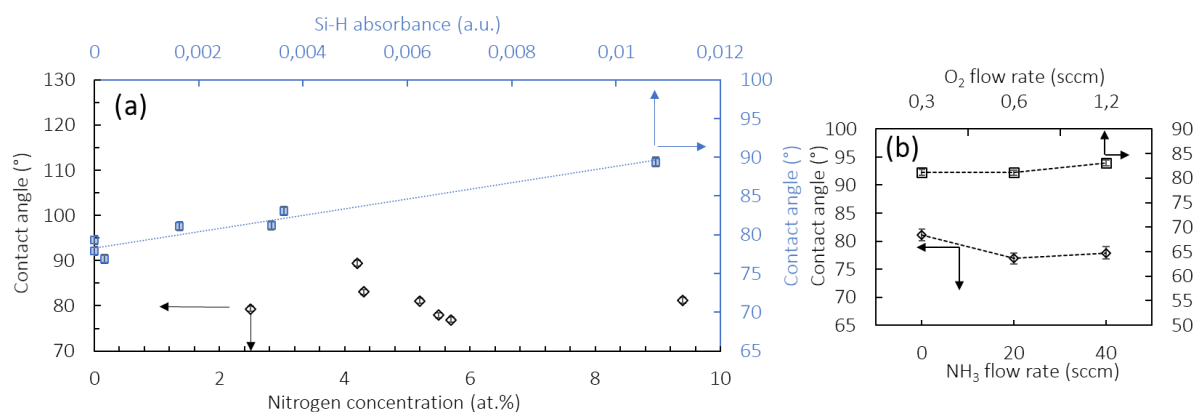


Figure 7. Water wettability results for  $\text{SiO}_x\text{N}_y$  films from various runs (TD6, TD8, TD7, TD11 and TD12). Evolution of the contact angle as a function of the nitrogen content and Si–H FT-IR absorption at ca.  $630\text{--}650\text{ cm}^{-1}$  (a), and  $\text{NH}_3$  flow rate and  $\text{O}_2$  flow rate in absence of  $\text{NH}_3$  (b). Trend lines serving as guide to the eyes.

The wettability behavior of these films is segregated and examined as a function of their respective process parameters. More specifically, Figure 7(b) shows the change in WCA for increasing  $\text{NH}_3$  supply under a fixed  $\text{O}_2$  supply (runs TD6, TD7, TD8), and for increasing  $\text{O}_2$  flow rate in absence of ammonia (runs TD7, TD11, TD12). In the first dataset, higher  $\text{NH}_3$  supply appears to decrease the WCA. This may be assigned to  $-\text{CH}_3$  cleaving of organic moieties by  $\text{NH}_3$  and reduction in carbon as was revealed by IBA (Figure 2(a)), the presence of which conventionally increases the hydrophobic character of the films.<sup>65–67</sup> An alternative interpretation is likely the insertion of further surface  $-\text{N}-\text{H}_x$  bonds in the films for higher  $\text{NH}_3$  supply. Si–NH–Si bonds are hydrophilic given their polarity and quick reaction with air humidity.<sup>66</sup> No correlation was noted however when plotting the WCA as a function of the N–H  $3300\text{--}3400\text{ cm}^{-1}$  infrared absorption.

An increase of the  $\text{O}_2$  supply in ammonia-free experiments (runs TD7, TD11, TD12) slightly increases the WCA (Figure 7(b)). This behavior is unexpected, since higher  $\text{O}_2$  supply decreases N incorporation and enhances the oxide character of the material, reported to facilitate dipole interaction



and hydrogen bonding between Si-OH and H<sub>2</sub>O, resulting in more negatively charged and hydrophilic surfaces.<sup>68</sup> The slight increase in WCA is thus difficult to explain, but could be related to a replacement of hydrophilic NH<sub>x</sub> groups by slightly less hydrophilic Si-OH ones.

Although only two points were analyzed, the effect of the deposition temperature is also considered (Figure SI7 of *Supplementary Information*). A lower contact angle is noted, although this result cannot be attributed solely to the deposition temperature and may be also linked to the higher N concentration and by extension higher amount of hydrophilic NH<sub>x</sub> bonds. Overall, given the multi-factorial dependency of the wettability behavior on the surface termination, composition and surface roughness, the WCA results cannot be explained solely as a function of isolated deposition conditions.

#### *Wet etching corrosion resistance*

The wet etching corrosion resistance of SiO<sub>x</sub>N<sub>y</sub> films is presented in Figure 8. The evolution of the BOE 6:1 etching rate of films produced from various runs is shown in Figure 8(a), plotted as a function of their nitrogen content. An overall decreasing trend is noted, with the etching rate being reduced as the nitrogen content of the films increases. A maximum etching rate of 74.6 Å.s<sup>-1</sup> is measured for SiO<sub>x</sub>N<sub>y</sub> films with low nitrogen incorporation, decreasing to near-zero values of 0.1 Å.s<sup>-1</sup> for films with higher composition in nitrogen. The power curve added for visual aid reveals a convergence to values below 4 Å.s<sup>-1</sup> beyond ca. 7 at.% N. It can be proposed that, for the tested conditions, ca. 7 at.% N is sufficient in providing an excellent corrosion resistance and that further N incorporation beyond this value is not necessary. Such information is important for the definition of operating conditions that are aimed at to produce films with a targeted corrosion resistance behavior.

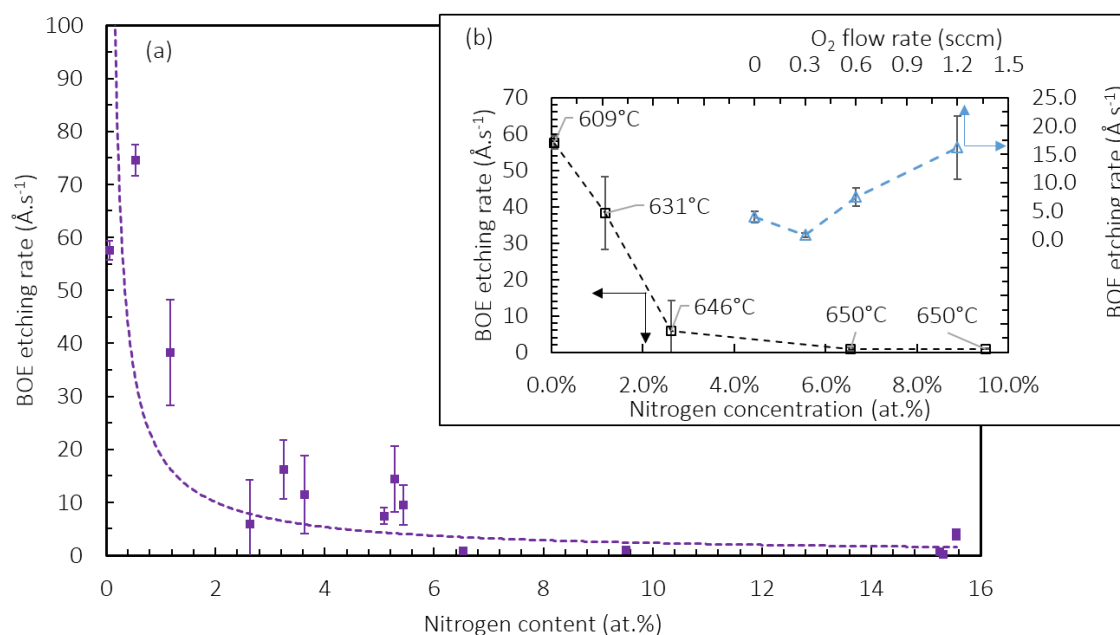


Figure 8. Evolution of the BOE etching rate as a function of the nitrogen content, for samples deposited at various conditions (a), for samples of run TD3 (empty black squares) and for samples deposited for varying O<sub>2</sub> flow rates (blue triangles) (b). Trend lines added as guide for the eyes.

Since the etching rates of Figure 8(a) were measured from films produced from a variety of operating conditions, the values are examined separately to investigate how the specific process parameters affect the etching rate. Figure 8(b) shows the etching rate evolution of 5 samples (pH, pJ, pL, p3, p6) taken from run TD3 produced at different positions in the reactor with distinct local temperatures, plotted as a function of their nitrogen content. The local temperature of each sample is also included. For a sample with 0.1 at.% N produced at a local temperature of 609°C outside the isothermal region, the BOE etching rate is 57.5 Å.s<sup>-1</sup>. In contrast, a sample with 9.5 at.% N taken from the isothermal region (local temperature of 650°C) exhibit an etching rate of 0.9 Å.s<sup>-1</sup>. Similar overall reductions are observed for a simultaneous increase in temperature and nitrogen content. Additionally, the evolution of Figure 8(b) presents a break in its slope: a steep decrease in the 0-2.5 at.% N range is noted, attributed to the temperature effect. Between 2.5 and 10 at.% N the slope appears milder, with the temperature remaining constant for these samples. Thus, although the etching rate seems to depend strongly on the process temperature, it must be recalled that this process parameter also influences the level of N incorporation.

Figure 8(b) also examines the effect of the O<sub>2</sub> flow rate on the BOE etching rate. When no O<sub>2</sub> is added in the inlet gas composition, a BOE etching rate of 3.9 Å.s<sup>-1</sup> is noted. An increase of the O<sub>2</sub> flow rate to 0.6 sccm results in a moderate increase of the BOE etching rate to 7.4 Å.s<sup>-1</sup>. This value increases sharply to 16.2 Å.s<sup>-1</sup> for an O<sub>2</sub> supply of 1.2 sccm, and the reduced corrosion resistance is correlated to

the higher oxide and loss in nitride character. Similar results were reported for  $\text{Si}_3\text{N}_4$ -to- $\text{SiO}_2$  films produced with an increasing addition of  $\text{O}_2$  in the inlet gas composition, where BOE etching rates increased dramatically up to 83 times with gradual increase in O incorporation.<sup>69</sup> Resistance to wet chemical etching is therefore strongly linked to the structural modifications brought about by the O/N substitution. Further N incorporation increases the overall compactness and rigidity of the network as it changes towards RMM.

### Surface roughness

The surface roughness of the films was examined by atomic force microscopy before and after subjection to the BOE 6:1 solution. As presented in Figure 9, the produced  $\text{SiO}_x\text{N}_y$  films are smooth with uniform surfaces. Their root mean square (RMS) roughness decreases from 1.05 to 0.62 nm with increasing nitrogen, showing an asymptote beyond 6 at.% N. A similar decreasing trend was noted by Tang et al.,<sup>60</sup> who reported a RMS decrease from 1.33 to 0.97 nm with parallel increase of the nitrogen content. In the present work, the RMS roughness also follows an increasing trend with increase of the deposition rate of the individual samples, independently of the deposition conditions (results not shown).

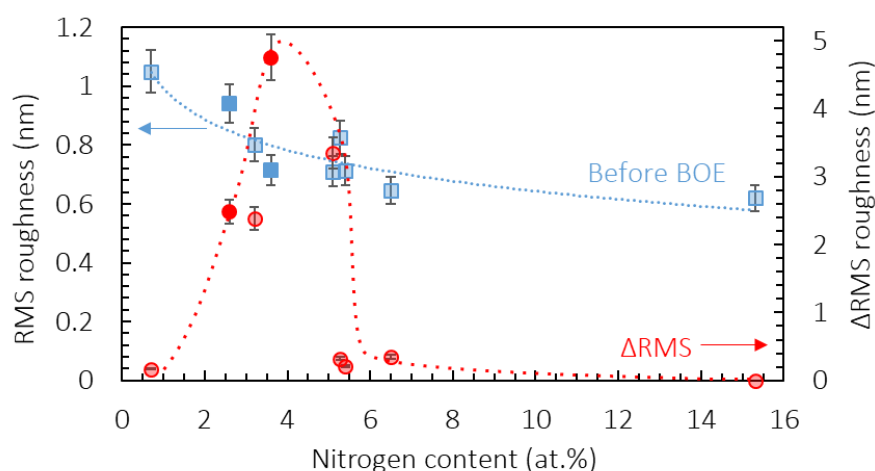


Figure 9. Evolution of the RMS roughness of  $\text{SiO}_x\text{N}_y$  before subjection to etching by the BOE solution (blue squares) and  $\Delta\text{RMS}$  roughness after BOE (red circles), produced at various conditions. Solid symbols refer to samples that were produced at temperatures below 650°C. Trend lines added as visual aid.

After subjection to the BOE etching solution, the RMS roughness is noted to increase for films containing up to 5 at.% N, as noted by the  $\Delta\text{RMS}$  roughness. No singular behavior is observed in this

region however. Starting with a sharp increase from 0.2 to 4.8 nm, the  $\Delta$ RMS roughness decreases back to 0.2 nm when the N content is increased from 4 to 5 at.%. Delta values below 0.2 nm are noted once the film composition surpasses 5 at.% N, in agreement with the limited sensitivity of these films to the corrosion test. Plotting of the post-BOE or delta RMS roughness as a function of the deposition rate or the particular deposition conditions, such as temperature or addition of  $\text{NH}_3$  in the starting inlet composition, did not reveal any correlation. The results indicate a difference in etching mechanism, strongly linked to the short-range order. Corrosion resistance is globally improved upon further addition of nitrogen as illustrated in Figure 8(a), yet results in a non-uniform etching profile. Interaction between the etching solution and the extreme sample surface appears to be dependent on the particular  $\text{O}_x\text{-Si-N}_y$  tetrahedral configuration of the atoms in the network, resulting in a quasi site-selective etching that is likely more pronounced in regions where the  $\text{O}_x\text{-Si-N}_y$  tetrahedra exhibit  $x > 2 > y$  or even  $y = 0$ . Moreover, it is recalled that a significant change in the C and N incorporation types was observed at around 5 at.% N, as revealed by FT-IR (Figure 3(e) and (f)). The presence of highly covalent Si-C bonds was reported to reinforce the nitride network, resulting in improved etching resistance.<sup>70</sup> In contrast, organic carbon (e.g.  $-\text{CH}_3$ ,  $-\text{CH}_x$ ,  $-\text{C}=\text{O}$ ) as observed by FT-IR and XPS in the present work, could be localized, given the C-rich areas revealed by HR-TEM (Figure SI5 of *Supporting Information*). This may lead to more etching-susceptible sites, increasing the RMS roughness.

## Conclusions

Given the tunable character of  $\text{SiO}_x\text{N}_y$  films and their attractiveness for numerous applications, especially those challenged by deposition at lower temperatures, it is pertinent to investigate the influence of the process parameters on the material properties. The thermal chemical vapor deposition of  $\text{SiO}_x\text{N}_y$  films from a new precursor, tris(dimethylsilyl)amine (TDMSA), was executed at 580–650°C, a thermal range lower compared to the ranges utilized for conventional disilazane precursors. A parametric analysis of composition trends was performed as a function of operating conditions such as  $\text{NH}_3$  and  $\text{O}_2$  flow rates and deposition temperature. It was demonstrated that higher  $\text{NH}_3$  supply decreases the film C content. For the studied range of parameters, deposition rate and film N content remained insensitive to variations of the ammonia flow rate, yielding films with maximum 7.5 at.% N. Inclusion of  $\text{NH}_3$  in the starting chemistry was not mandatory for the production of  $\text{SiO}_x\text{N}_y$  films, thanks to the role of the TDMSA precursor as a dual Si and N source. In the case of  $\text{O}_2$ , higher supply promoted O-rich film formation, with a competition existing between O and N incorporation.

Compositional trends highlighted by spectroscopic ellipsometry were confirmed using ion beam analyses. The produced films were hydrated, with hydrogen being involved in Si-OH,  $\text{CH}_3$ ,  $\text{CH}_x$ , and N-H moieties as revealed by FT-IR. The films were generally amorphous, globally described as a  $\text{SiO}_x\text{N}_y$

network, occasionally enriched locally in C and N. The organic character of the incorporated carbon and the low percentage of carbidic Si-C configuration was confirmed using XPS. The electron configuration revealed a substantial change in the bonding state of the atoms depending on the process conditions. Primarily, a shift from Si-N-H<sub>2</sub> and Si-O-N-Si<sub>2</sub> towards N-Si<sub>3</sub> with decreasing O<sub>2</sub> flow rate was highlighted, indicating a shift toward a random mixture model (RMM) of homogeneously mixed oxide and nitride configurations.

Simultaneously, the evolution of various film properties reflected the transition in the network structure. Evolution trends could arbitrarily be defined at 2 or 3 distinct levels, depending on the studied property. Globally, an increase in the nitrogen content resulted in an easily observable transitional region detected in the 3-6 at.% N range, within which material properties follow non-linear trends. Beyond ca. 6-7 at.% N, properties such as the film hardness, elastic modulus, surface roughness and etching rate adhered to linear behaviors again and appeared to converge to constant values. Other properties on the other hand, such as film adhesion established through nanoscratch critical load, present a dramatic increase beyond 7 at.% N. Incorporation of C and H atoms could play a significant role in the evolution of these transitional regions. Increased RMS roughness in the 3-5 at.% N range after subsection to hydrofluoric solution further supports the influence of the particular tetrahedral configuration and medium-range order on the material properties. Potential site-selective etching induced by regions rich in O, H and/or organic C is assumed.

Despite the presence of C and H, the produced SiO<sub>x</sub>N<sub>y</sub> films exhibited excellent resistance to wet etching corrosion in BOE 6:1 solution, with very low etching rates (0.1 Å.s<sup>-1</sup>) noted for films with >7 at.% N. Definition of this minimum required value is helpful for framing appropriate deposition parameters for etch-resistant SiO<sub>x</sub>N<sub>y</sub> films applied as wet corrosion protective coatings or etch-stop liner layers. The illustrated methodology serves as a demonstration for linking film composition, structure and properties to the CVD process conditions, and engineering amorphous SiO<sub>x</sub>N<sub>y</sub> films tailored for the envisioned applications.

Supporting Information: Schematic representation of experimental setup, FT-IR absorptions encountered in the produced SiO<sub>x</sub>N<sub>y</sub> films and their deconvolution, atomic concentrations of binding states for N 1s, C 1s, O 1s and Si 2p XPS spectra after deconvolution and EELS Spectrum-Imaging details.

## Acknowledgements

This work was supported by the Agence Nationale de la Recherche (ANR) under the contract HEALTHYGLASS ANR-17-CE08-0056. This project has benefited from the facilities of the platform MACLE-CVL. This platform was co-funded by the European Union, the Region – Centre Val de Loire and The French minister of research (MESRI – DRRT). Europe is committed to the Centre-Val de Loire region with the European regional development fund (ERDF). The authors are indebted to Olivier Debieu, Olivier Marsan and Claudie Josse for their advice and assistance with spectroscopic ellipsometry, FT-IR and FIB techniques, respectively.

## References

1. Alford, N.; Amouroux, J.; Barbier, D.; Bauer, G.; Borg, A.; Conde, J. P.; Gonzalez-Eliphe, A.; Grimmeiss, H.; Jäger-Waldau, A.; Jarvis, D.; Lippert, T.; Maier, S.; Müssig, H.-J.; Olsson, E.; Perrière, J.; Pfitzner, L.; Priolo, F.; Richter, H.; Ritschkoff, A. C.; Vahlas, C., *Materials for Key Enabling Technologies*. **2011**, pp. 26, 37.
2. Shi, Y.; He, L.; Guang, F.; Li, L.; Xin, Z.; Liu, R., A review: preparation, performance, and applications of silicon oxynitride film. *Micromachines* **2019**, *10* (8), 552.
3. Šimurka, L.; Čtvrtlík, R.; Roch, T.; Turutoğlu, T.; Erkan, S.; Tomašík, J.; Bange, K., Effect of deposition conditions on physical properties of sputtered silicon oxynitride thin films on float glass. *Int. J. Appl. Glass Sci.* **2018**, *9* (3), 403-412.
4. Wong, H.; Iwai, H., On the scaling issues and high-kappa replacement of ultrathin gate dielectrics for nanoscale MOS transistors. *Microelectron. Eng.* **2006**, *83* (10), 1867-1904.
5. Palm, J.; Probst, V.; Brummer, A.; Stetter, W.; Tölle, R.; Niesen, T. P.; Visbeck, S.; Hernandez, O.; Wendl, M.; Vogt, H.; Calwer, H.; Freienstein, B.; Karg, F., CIS module pilot processing applying concurrent rapid selenization and sulfurization of large area thin film precursors. *Thin Solid Films* **2003**, *431-432*, 514-522.
6. Nishimura, A.; Matsuda, S.; Kabe, Y., The Temperature Coefficients of Frequency of Surface Acoustic Wave Devices With SiO<sub>x</sub>N<sub>y</sub> Passivation Films on LiTaO<sub>3</sub> Substrates. *IEEE Trans. Ultrason. Eng.* **2021**, *68* (5), 1965-1971.
7. Gupta, R.; Vaid, R., Structural and Electrical Characteristics of ALD-TiO<sub>2</sub>/SiON/n-Si Gate-Stack for Advanced CMOS Device Applications. *IEEE Trans. Electron Devices* **2021**, *68* (6), 2625-2632.
8. Barman, B. K.; Handegard, O. S.; Hernandez-Pinilla, D.; Shinde, S. L.; Nagao, T., Transparent Hard Coatings with SiON-Encapsulated N-Doped Carbon Dots for Complete UV Blocking and White Light Emission. *ACS Appl. Electron. Mater.* **2021**, *3* (9), 3761-3773.
9. Shahpanah, M.; Mehrabian, S.; Abbasi-Firouzjah, M.; Shokri, B., Improving the oxygen barrier properties of PET polymer by radio frequency plasma-polymerized SiO<sub>x</sub>N<sub>y</sub> thin film. *Surf. Coat. Technol.* **2019**, *358*, 91-97.

10. Chen, K.; Lin, Z.; Zhang, P.; Huang, R.; Dong, H.; Huang, X., Luminescence mechanism in amorphous silicon oxynitride films: band tail model or N-Si-O bond defects model. *Frontiers in Physics* **2019**, 7, 144.
11. Yadav, A. D.; Polji, R. H.; Singh, V.; Dubey, S. K.; Gundu Rao, T. K., Synthesis of buried silicon oxynitride layers by ion implantation for silicon-on-insulator (SOI) structures. *Nucl. Instrum. Methods Phys. Res., Sect. B* **2006**, 245 (2), 475-479.
12. Tomar, V.; Patil, D.; Gautam, D., Deposition and characterization of SiON films using HMDS for photonics applications. *Semicond. Sci. Technol.* **2006**, 22 (2), 43-48.
13. Kaghouché, B.; Mansour, F.; Molliet, C.; Rousset, B.; Temple-Boyer, P., Investigation on optical and physico-chemical properties of LPCVD SiO<sub>x</sub>N<sub>y</sub> thin films. *The European Physical Journal Applied Physics* **2014**, 66 (2), 20301.
14. Parsons, G. N.; Souk, J. H.; Batey, J., Low hydrogen content stoichiometric silicon nitride films deposited by plasma - enhanced chemical vapor deposition. *J. Appl. Phys.* **1991**, 70 (3), 1553-1560.
15. Lin, Y.-S.; Liao, Y.-H.; Weng, M.-S., Enhanced scratch resistance of polycarbonate by low temperature plasma-polymerized organosilica. *Thin Solid Films* **2009**, 517 (17), 5224-5230.
16. Walkiewicz-Pietrzykowska, A.; Cotrino, J.; González-Elipé, A. R., Deposition of Thin Films of SiO<sub>x</sub>C<sub>y</sub>H in a Surfatron Microwave Plasma Reactor with Hexamethyldisiloxane as Precursor. *Chem. Vap. Deposition* **2005**, 11 (6-7), 317-323.
17. Perani, M.; Brinkmann, N.; Fazio, M. A.; Hammud, A.; Terheiden, B.; Cavalcoli, D., Annealing effects on SiO<sub>x</sub>N<sub>y</sub> thin films: Optical and morphological properties. *Thin Solid Films* **2016**, 617, 133-137.
18. Decosterd, L.; Topka, K. C.; Diallo, B.; Samelor, D.; Vergnes, H.; Senocq, F.; Caussat, B.; Vahlas, C.; Menu, M.-J., An innovative GC-MS, NMR and ESR combined, gas-phase investigation during chemical vapor deposition of silicon oxynitrides films from tris(dimethylsilyl)amine. *Phys. Chem. Chem. Phys.* **2021**, 23 (17), 10560-10572.
19. Topka, K. C.; Vergnes, H.; Tsiros, T.; Papavasileiou, P.; Decosterd, L.; Diallo, B.; Senocq, F.; Samelor, D.; Pellerin, N.; Menu, M.-J.; Vahlas, C.; Caussat, B., An innovative kinetic model allowing insight in the moderate temperature chemical vapor deposition of silicon oxynitride films from tris(dimethylsilyl)amine. *Chem. Eng. J.* **2022**, 431, 133350.
20. Tomar, V.; Patil, D.; Gautam, D., Deposition and characterization of SiON films using HMDS for photonics applications. *Semicond. Sci. Technol.* **2006**, 22 (2), 43.
21. Topka, K. C.; Chliavoras, G. A.; Senocq, F.; Vergnes, H.; Samelor, D.; Sadowski, D.; Vahlas, C.; Caussat, B., Large temperature range model for the atmospheric pressure chemical vapor deposition of silicon dioxide films on thermosensitive substrates. *Chem. Eng. Res. Des.* **2020**, 161, 146-158.
22. Mayer, M., SIMNRA, a simulation program for the analysis of NRA, RBS and ERDA. *AIP Conference Proceedings* **1999**, 475, 541-544.
23. Diallo, B.; Topka, K. C.; Puyo, M.; Lebesgue, C.; Genevois, C.; Laloo, R.; Samelor, D.; Lecoq, H.; Allix, M.; Vergnes, H.; Senocq, F.; Florian, P.; Sarou-Kanian, V.; Sauvage, T.; Menu, M.-J.; Caussat, B.; Turq, V.; Vahlas, C.; Pellerin, N., Network hydration, ordering and composition interplay of chemical vapor deposited amorphous silica films from tetraethyl orthosilicate. *J. Mater. Res. Technol.* **2021**, 13, 534-547.



24. Ponton, S.; Dhainaut, F.; Vergnes, H.; Samelor, D.; Sadowski, D.; Rouessac, V.; Lecoq, H.; Sauvage, T.; Caussat, B.; Vahlas, C., Investigation of the densification mechanisms and corrosion resistance of amorphous silica films. *J. Non-Cryst. Solids* **2019**, *515*, 34–41.
25. Topka, K. C.; Diallo, B.; Samelor, D.; Laloo, R.; Sadowski, D.; Genevois, C.; Sauvage, T.; Senocq, F.; Vergnes, H.; Turq, V.; Pellerin, N.; Caussat, B.; Vahlas, C., Tunable SiO<sub>2</sub> to SiO<sub>x</sub>C<sub>y</sub>H films by ozone assisted chemical vapor deposition from tetraethylorthosilicate and hexamethyldisilazane mixtures. *Surf. Coat. Technol.* **2021**, *407*, 126762.
26. Oliver, W. C.; Pharr, G. M., An improved technique for determining hardness and elastic modulus using load and displacement sensing indentation experiments. *J. Mater. Res.* **2011**, *7* (6), 1564–1583.
27. Gao, M.; Zhao, Z. J.; Kim, H.; Jin, M. L.; Li, P.; Kim, T.; Kang, K.; Cho, I.; Jeong, J. H.; Park, I., Buffered Oxide Etchant Post-Treatment of a Silicon Nanofilm for Low-Cost and Performance-Enhanced Chemical Sensors. *ACS Appl. Mater. Interfaces* **2020**, *12* (33), 37128–37136.
28. Cova, P.; Masut, R. A.; Grenier, O.; Poulin, S., Effect of unintentionally introduced oxygen on the electron–cyclotron resonance chemical-vapor deposition of SiN<sub>x</sub> films. *J. Appl. Phys.* **2002**, *92* (1), 129–138.
29. Lee, J. H.; Jeong, C. H.; Lim, J. T.; Zavaleyev, V. A.; Kyung, S. J.; Yeom, G. Y., SiO<sub>x</sub>N<sub>y</sub> thin film deposited by plasma enhanced chemical vapor deposition at low temperature using HMDS–O<sub>2</sub>–NH<sub>3</sub>–Ar gas mixtures. *Surf. Coat. Technol.* **2007**, *201* (9–11), 4957–4960.
30. Fainer, N. I.; Kosinova, M. L.; Maximovsky, E. A.; Rumyantsev, Y. M.; Kuznetsov, F. A.; Kesler, V. G.; Kirienko, V. V., Study of the structure and phase composition of nanocrystalline silicon oxynitride films synthesized by ICP-CVD. *Nucl. Instrum. Methods Phys. Res., Sect. A* **2005**, *543* (1), 134–138.
31. Weiller, B. H., Chemical Vapor Deposition of TiN from Tetrakis(dimethylamido)titanium and Ammonia: Kinetics and Mechanistic Studies of the Gas-Phase Chemistry. *J. Am. Chem. Soc.* **1996**, *118* (21), 4975–4983.
32. Ray, S. K.; Maiti, C. K.; Chakrabarti, N. B., Low-Temperature deposition of dielectric films by microwave plasma enhanced decomposition of hexamethyldisilazane. *J. Electron. Mater.* **1991**, *20* (11), 907–913.
33. Farhaoui, A.; Bousquet, A.; Smaali, R.; Moreau, A.; Centeno, E.; Cellier, J.; Bernard, C.; Rapegno, R.; Réveret, F.; Tomasella, E., Reactive gas pulsing sputtering process, a promising technique to elaborate silicon oxynitride multilayer nanometric antireflective coatings. *J. Phys. D: Appl. Phys.* **2016**, *50* (1), 015306.
34. Habraken, F. H. P. M.; Kuiper, A. E. T., Silicon nitride and oxynitride films. *Mater. Sci. Eng., R* **1994**, *12* (3), 123–175.
35. Taraskin, S. N.; Elliott, S. R., Nature of vibrational excitations in vitreous silica. *Phys. Rev. B* **1997**, *56* (14), 8605–8622.
36. Nagasawa, H.; Minamizawa, T.; Kanezashi, M.; Yoshioka, T.; Tsuru, T., Microporous organosilica membranes for gas separation prepared via PECVD using different O/Si ratio precursors. *J. Membr. Sci.* **2015**, *489*, 11–19.
37. Ay, F.; Aydinli, A., Comparative investigation of hydrogen bonding in silicon based PECVD grown dielectrics for optical waveguides. *Opt. Mater.* **2004**, *26* (1), 33–46.



38. Hallam, B.; Tjahjono, B.; Wenham, S., Effect of PECVD silicon oxynitride film composition on the surface passivation of silicon wafers. *Sol. Energy Mater. Sol. Cells* **2012**, *96*, 173-179.
39. Giorgis, F.; Giuliani, F.; Pirri, C.; Tresso, E.; Summonte, C.; Rizzoli, R.; Galloni, R.; Desalvo, A.; Rava, P., Optical, structural and electrical properties of device-quality hydrogenated amorphous silicon-nitrogen films deposited by plasma-enhanced chemical vapour deposition. *Phil. Mag. B* **1998**, *77* (4), 925-944.
40. Yin, Z.; Smith, F., Optical dielectric function and infrared absorption of hydrogenated amorphous silicon nitride films: Experimental results and effective-medium-approximation analysis. *Phys. Rev. B* **1990**, *42* (6), 3666.
41. Nakamura, K.; Nonaka, H.; Kameda, N.; Nishiguchi, T.; Ichimura, S., Photochemical Reaction of Ozone and 1,1,1,3,3,3-Hexamethyldisilazane: Analysis of the Gas Reaction between Precursors in a Photochemical Vapor Deposition Process. *Japanese J. Appl. Phys.* **2008**, *47* (9), 7349-7355.
42. Launer, P. J., Infrared analysis of organosilicon compounds: spectra-structure correlations. In *Silicone compounds register and review*, Petrarch Systems Bristol, PA, 1987; Vol. 100.
43. Bensch, W.; Bergholz, W., An FT-IR study of silicon dioxides for VLSI microelectronics. *Semicond. Sci. Technol.* **1990**, *5* (5), 421.
44. Trunec, D.; Navrátil, Z.; Stahel, P.; Zajíková, L.; Buráková, V.; Cech, J., Deposition of thin organosilicon polymer films in atmospheric pressure glow discharge. *J. Phys. D: Appl. Phys.* **2004**, *37* (15), 2112-2120.
45. Bulou, S.; Le Brizoual, L.; Miska, P.; de Pouques, L.; Hugon, R.; Belmahi, M.; Bougdira, J., The influence of CH<sub>4</sub> addition on composition, structure and optical characteristics of SiCN thin films deposited in a CH<sub>4</sub>/N<sub>2</sub>/Ar/hexamethyldisilazane microwave plasma. *Thin Solid Films* **2011**, *520* (1), 245-250.
46. Pecora, A.; Maiolo, L.; Fortunato, G.; Caligiore, C., A comparative analysis of silicon dioxide films deposited by ECR-PECVD, TEOS-PECVD and Vapox-APCVD. *J. Non-Cryst. Solids* **2006**, *352* (9-20), 1430-1433.
47. Ngamou, P. H. T.; Overbeek, J. P.; Kreiter, R.; van Veen, H. M.; Vente, J. F.; Wienk, I. M.; Cuperus, P. F.; Creatore, M., Plasma-deposited hybrid silica membranes with a controlled retention of organic bridges. *J. Mater. Chem. A* **2013**, *1* (18), 5567-5576.
48. Behrens, K. M.; Klinkenberg, E. D.; Finster, J.; Meiwes-Broer, K. H., Geometric structure of thin SiO<sub>x</sub>N<sub>y</sub> films on Si(100). *Surface Sci.* **1998**, *402-404*, 729-733.
49. Bustarret, E.; Bensouda, M.; Habrard, M. C.; Bruyère, J. C.; Poulin, S.; Gujrathi, S. C., Configurational statistics in a-Si<sub>x</sub>N<sub>y</sub>H<sub>z</sub> alloys: A quantitative bonding analysis. *Phys. Rev. B* **1988**, *38* (12), 8171-8184.
50. Scardera, G.; Bellet-Amalric, E.; Bellet, D.; Puzzer, T.; Pink, E.; Conibeer, G., Formation of a Si-Si<sub>3</sub>N<sub>4</sub> nanocomposite from plasma enhanced chemical vapour deposition multilayer structures. *J. Cryst. Gr.* **2008**, *310* (15), 3685-3689.
51. Yonekura, D.; Fujikawa, K.; Murakami, R.-I., Influence of film structure on gas barrier properties of SiO<sub>x</sub>N<sub>y</sub> films. *Surf. Coat. Technol.* **2010**, *205* (1), 168-173.
52. Lo, T.-Y.; Huang, Y.-C.; Hsiao, Y.-N.; Chao, C.-G.; Whang, W.-T., Preparation of superhydrophobic polyimide films modified with organosilicasol as effective anticorrosion coatings. *Surf. Coat. Technol.* **2014**, *258*, 310-319.

53. Nakaya, M.; Yasuhara, S.; Maeda, T.; Hotta, A., Impact of hot wire and material gas species on the Cat-CVD coating of gas barrier SiOC thin films onto PET bottles. *Surf. Coat. Technol.* **2018**, *344*, 21-29.
54. Oulachgar, E. H.; Aktik, C.; Dostie, S.; Sowerby, R.; Gujrathi, S.; Scarlete, M., Chemical and Structural Characterization of SiONC Dielectric Thin Film Deposited by PSCVD. *J. Electrochem. Soc.* **2006**, *153* (11), F255-F259.
55. Chainani, A.; Nema, S.; Kikani, P.; John, P., Electronic structure of carbon-free silicon oxynitride films grown using an organic precursor hexamethyl-disilazane. *J. Phys. D: Appl. Phys.* **2002**, *35* (11), L44.
56. Zhang, P.; Chen, K.; Dong, H.; Zhang, P.; Fang, Z.; Li, W.; Xu, J.; Huang, X., Higher than 60% internal quantum efficiency of photoluminescence from amorphous silicon oxynitride thin films at wavelength of 470 nm. *Appl. Phys. Lett.* **2014**, *105* (1), 011113.
57. Fainer, N. I.; Kosinova, M. L.; Rumyantsev, Y. M.; Maximovskii, E. A.; Kuznetsov, F. A., Thin silicon carbonitride films are perspective low-k materials. *J. Phys. Chem. Solids* **2008**, *69* (2-3), 661-668.
58. Shallenberger, J. R.; Cole, D. A.; Novak, S. W., Characterization of silicon oxynitride thin films by x-ray photoelectron spectroscopy. *J. Vac. Sci. Technol., A* **1999**, *17* (4), 1086-1090.
59. Daldosso, N.; Luppi, M.; Ossicini, S.; Degoli, E.; Magri, R.; Dalba, G.; Fornasini, P.; Grisenti, R.; Rocca, F.; Pavesi, L., Role of the interface region on the optoelectronic properties of silicon nanocrystals embedded in SiO<sub>2</sub>. *Phys. Rev. B* **2003**, *68* (8), 085327.
60. Tang, C.-J.; Jaing, C.-C.; Tien, C.-L.; Sun, W.-C.; Lin, S.-C., Optical, structural, and mechanical properties of silicon oxynitride films prepared by pulsed magnetron sputtering. *Appl. Opt.* **2017**, *56* (4), C168-C174.
61. Gan, Z.; Wang, C.; Chen, Z., Material Structure and Mechanical Properties of Silicon Nitride and Silicon Oxynitride Thin Films Deposited by Plasma Enhanced Chemical Vapor Deposition. *Surfaces* **2018**, *1* (1), 59-72.
62. Trevino, K. J.; Shearer, J. C.; McCurdy, P. R.; Pease-Dodson, S. E.; Okegbe, C. C.; Fisher, E. R., Isoelectric points of plasma-modified and aged silicon oxynitride surfaces measured using contact angle titrations. *Surf. Interface Anal.* **2011**, *43* (9), 1257-1270.
63. Tsukruk, V. V.; Bliznyuk, V. N., Adhesive and Friction Forces between Chemically Modified Silicon and Silicon Nitride Surfaces. *Langmuir* **1998**, *14* (2), 446-455.
64. Zhang, X.; Ptasinska, S., Growth of silicon oxynitride films by atmospheric pressure plasma jet. *J. Phys. D: Appl. Phys.* **2014**, *47* (14), 145202.
65. Arafat, A.; Schroën, K.; de Smet, L. C.; Sudhölter, E. J.; Zuilhof, H., Tailor-made functionalization of silicon nitride surfaces. *J. Am. Chem. Soc.* **2004**, *126* (28), 8600-8601.
66. Zhang, Z.; Shao, Z.; Luo, Y.; An, P.; Zhang, M.; Xu, C., Hydrophobic, transparent and hard silicon oxynitride coating from perhydropolysilazane. *Polymer International* **2015**, *64* (8), 971-978.
67. Saengdee, P.; Chaisriratanakul, W.; Bunjongpru, W.; Sripumkhai, W.; Srisuwan, A.; Jeamsaksiri, W.; Hruanun, C.; Poyai, A.; Promptmas, C., Surface modification of silicon dioxide, silicon nitride and titanium oxynitride for lactate dehydrogenase immobilization. *Biosens. Bioelectron.* **2015**, *67*, 134-138.

68. Hong, J.; Kim, Y.; Paik, H.; No, K.; Lukes, J. R., The effect of nitrogen incorporation on surface properties of silicon oxynitride films. *Phys. Status Solidi RRL* **2009**, 3 (1), 25-27.
69. Volkov, V. T.; Satunkina, L. F., Influence of oxygen on the composition and some properties of the films obtained by r.f. sputtering from a  $\text{Si}_3\text{N}_4$  target. *Thin Solid Films* **1994**, 247 (2), 145-147.
70. Gumphier, J.; Bather, W.; Mehta, N.; Wedel, D., Characterization of low-temperature silicon nitride LPCVD from bis (tertiary-butylamino) silane and ammonia. *J. Electrochem. Soc.* **2004**, 151 (5), G353.

## For Table of Contents Only

